Published as:
Nucl. Fusion **64**, 036003 (2024)
https://doi.org/10.1088/1741-4326/ad1e94

Quasi-mode Evolution in a Stochastic Magnetic Field

Mingyun Cao and P.H. Diamond

Department of Physics, University of California, San Diego,
La Jolla, CA 92093, United States of America

E-mail: m2cao@ucsd.edu

June 2023

Abstract. We present a multi-scale model of quasi-mode evolution in a stochastic magnetic field. The similarity between a quasi-mode and a ballooning mode enables us to address the challenges arising from the disparate geometries in the theories of ballooning modes in the presence of resonant magnetic perturbations. We obtain useful insights into our understanding of ballooning mode dynamics in a stochastic background. To maintain quasi-neutrality at all scales, the beat between the quasi-mode and the stochastic magnetic field drives microturbulence, which drives the turbulent background that promotes mixing and damps the quasi-mode. As a result of the broad mode structure of the quasi-mode, the turbulent viscosity and the turbulent diffusivity produced by the microturbulence are larger than those in our related study on resistive interchange modes. The stochastic magnetic field can also enhance the effective plasma inertia and reduce the effective drive, thereby slowing the mode growth. A nontrivial correlation between the microturbulence and the magnetic perturbations is shown to develop. This could account for the reduction in the Jensen-Shannon complexity of pedestal turbulence in the RMP ELM suppression phase observed in recent experiments. Directions for future experimental and theoretical studies are suggested.

Keywords: ballooning mode, quasi-mode, stochastic magnetic fields, microturbulence, complexity-entropy analysis

1. Introduction

Future magnetic confinement fusion reactors, such as ITER [1], are designed to operate in the high-confinement mode for good plasma performance. As a result, dealing with the edge-localized mode (ELM)—a "side effect" of the H-mode—is one of the major concerns in fusion science today. In experiments, a technique called resonant magnetic perturbation (RMP) is widely adopted to mitigate and suppress ELMs by generating a stochastic magnetic field at the plasma edge [2, 3]. However, as turbulence evolution and transport bifurcation now happen in a background stochastic field, an increase in the L-H transition power threshold has been observed on multiple machines [4, 5, 6]. To get insight into the tripartite trade-off among confinement, heating power, and boundary control, models of turbulence dynamics [7], zonal flow evolution [8], and L-H transition [9] have been reformulated in the presence of extrinsic stochasticity. All these theories are either based on or closely relevant to a fundamental question: how does an ambient stochastic magnetic field modify plasma turbulence and the underlying instability process? This paper entrances previous work on this subject [10] by delving deeper into the geometric complexities.

Experiments play a critical role in illuminating this question. Many intriguing phenomena, such as the significant reduction in the edge plasma density (density pump-out), form part of our current understanding of plasma confinement with the influence of RMP. In addition, there has been some progress in experimental studies on the effects of stochastic magnetic fields on plasma turbulence. For instance, an increase in the pedestal fluctuation level is observed in the RMP ELM suppression phase [11]. However, due to the technical difficulty in turbulence diagnostics, these studies primarily rely on the spectral analysis, which alone fails to fully capture the changes in the states of turbulence when RMP is implemented. Given that plasma turbulence is intermittent, more information is needed to characterize the effects of stochastic magnetic fields on its statistical behaviors.

In information theory, complexity-entropy analysis is a useful method that can quantify the predictability and structural intricacy of time series and signals. In this approach, Jensen-Shannon complexity C_{JS} serves as a metric of a system's complexity, which is defined as

$$C_{\mathrm{JS}} = HQ. \tag{1}$$

Here H is the permutation entropy, a measure of the missing information of a system, and Q is the Jensen-Shannon divergence, a measure of the distance of a system from thermal equilibrium state. C_{JS}, H and Q are all functionals of the signals recorded. As a side note, it can be proved that this permutation entropy H coincides with the Kolmogorov–Sinai entropy for piecewise monotone interval maps [12]. One important feature of this approach is its user-friendliness. For a time series obtained from experiments, the calculation of its Jensen-Shannon complexity is much simpler compared to other metrics, for example, the Kolmogorov-Sinai entropy [13]. Another advantage of this definition is that the number given by C_{JS} aligns with people's intuitive perception of a system's complexity. For instance, the Jensen-Shannon complexity metric reflects the widely-held notion that both the white noise and perfect crystals are 'simple' systems. Specifically, the white noise has a high entropy but low complexity, because there is no discernible structure. In contrast, a perfect crystal has low entropy and also low complexity, as it is perfectly regular. Generally, deterministic chaotic systems, such as the logistic map, always have high complexity, while noisy signals, like Brownian motion, are associated with low complexity [14]. This fact enables us to distinguish chaos from noise. Consequently, complexity-entropy analysis has been applied to various areas, including hydrology [15], economy [16], semantics [17], etc. As a special case of chaos, turbulence is intrinsically different from noise: the former exhibits a spectral energy flux in the k-space, while the energy emission and absorption in the latter case are *local* in k. Given the significance of turbulence in MFE, the complexity-entropy analysis has also been noticed by the fusion community. Using this approach, the chaotic nature of the edge fluctuations in L-mode, H-mode, and I-mode has been identified [18, 19, 20]. However, as reported by Choi et al., the rescaled Jensen-Shannon complexity of the temperature fluctuations at the pedestal top in the RMP ELM suppression phase is *reduced* relative to that in the natural ELM-free phase and the RMP ELM mitigation phase [21]. *This indicates that the edge plasma turbulence becomes more "noisy" when ELM is suppressed by RMP.* A fundamental change in the statistical dynamics of the turbulence due to stochastic field is thus implied. Additionally—and somewhat paradoxically—an *increase* in the bicoherence of the pedestal turbulence was also observed when system entered the RMP ELM suppression regime, as shown in figure 1. These observations further underscore the necessity of studying the fundamentals of plasma instabilities and turbulence in a stochastic magnetic field.

In our previous work [10], we probed this question by developing a multi-scale model which maintains $\nabla \cdot \boldsymbol{J} = 0$ at all scales. The chosen object of that research is the resistive interchange mode [22, 23, 24], primarily due to its tractability. While that model provides

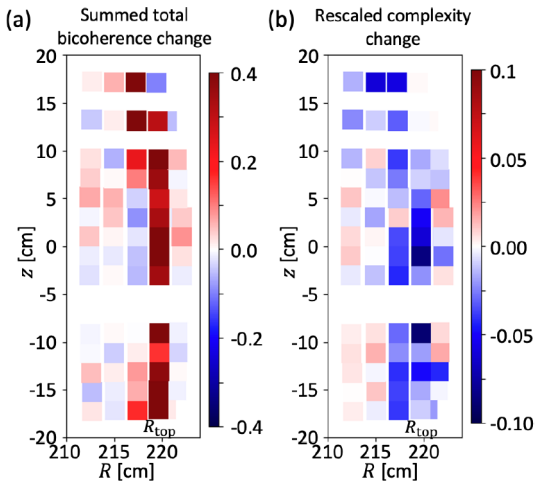

Figure 1. Changes of the summed total bicoherence (a) and rescaled complexity (b) of the electron temperature fluctuation between the ELM mitigation and the initial suppression phases. Reprinted from [21].

generic and *valuable* physical insights, its quantitative results may not be especially convincing, due to the geometric simplicity of the interchange modes. As the peeling-ballooning mode is a probable candidate for the origin of ELM [25], the ballooning mode is a more relevant instability to examine. However, apart from the inherent higher complexity of the ballooning mode (compared to the interchange mode), there is another hard nut to crack: *while models for ballooning modes in a tokamak are set up in toroidal geometry* [26], *theories involving resonant magnetic perturbations often are formulated in terms of resonant surfaces in a cylindrical geometry* [27]. To develop a comprehensive theory that encompasses both the ballooning mode and RMP, these two different geometries must be reconciled. For a stellarator, due to the lack of the toroidal symmetry, system is fully three-dimensional [28]. Therefore, theories of ballooning mode [29, 30] and resonant magnetic perturbations [31, 32] have been established in fully three-dimensional geometries. Meanwhile, codes for MHD simulations are extended to the stellarator geometry, such as M3D-C[1] [33], are developed. While it may seem that there is no problem of geometry disparity in the case of stellarator, a direct theoretical study on the ballooning mode in a stochastic magnetic field in a fully three-dimensional geometry is intimidating and intractable. To get results which may be readily understood, we need to compromise on the geometric complexity and choose to study this reduced problem. For the reasons given above, in this work, we will work on the cylindrical geometry model, and the strategy for the geometry reconciliation is to replace the ballooning mode with its counterpart in a cylinder, i.e., the quasi-mode. Figure 2 is an illustration of the mode structures of the quasi-mode and the ballooning mode. It can be seen from figure 2(a) that a quasi-mode, denoted by red envelope curves, is composed of vertically localized (resistive) interchange modes, represented by yellow columns. Likewise, as shown in figure 2(b), a ballooning mode, denoted by the red dotted curve, is a coupling of localized poloidal harmonics (blue hills). Hence, we conclude that *a quasi-mode in a cylinder resembles a ballooning mode in a torus.* As both the quasi-mode and the stochastic magnetic field reside in a cylindrical geometry, studying a quasi-mode in a stochastic magnetic field is manageable.

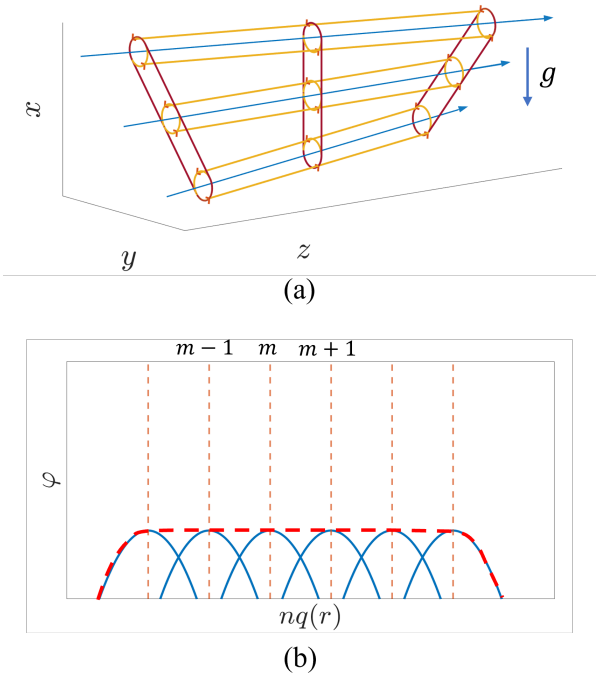

Figure 2. The similarity between quasi-mode and ballooning mode. (a) A depiction of the quasi-mode. The blue lines are magnetic field lines. The yellow columns are fluid filaments of gravitational interchange modes at different horizontal surfaces. The red envelope curves of these fluid filaments represent the convective cells of the quasi-mode. So a quasi-mode can be viewed as a wave-packet of gravitational interchange modes. (b) A simple sketch of the ballooning mode. The blue hills are poloidal harmonics localized at a sequence of resonant surfaces. Ballooning mode (red dotted curve) is a coupling of these harmonics due to toroidicity effect.

In this paper, we present a theory of the quasi-mode in a static, ambient stochastic magnetic field. We need to emphasize that here we mainly focus on the strong chaos regime, in which the Chirikov island overlap parameter is large, i.e.,

$$\sigma_{\text{Chirikov}} = \frac{\delta_{m,n} + \delta_{m',n'}}{\Delta_{m,n;m',n'}} \gg 1, \tag{2}$$

where $\delta_{m,n}$ and $\delta_{m',n'}$ are the half width of the magnetic islands at $q(r_{m,n}) = m/n$ and $q(r_{m',n'}) = m'/n'$ resonant surfaces, and $\Delta_{m,n,m',n'}$ is the distance between these two surfaces. This assumption indicates RMP current is relatively high in experiments. Hence, while the flux surfaces in the core remain unperturbed, the edge stochastic magnetic field can be regarded as strongly chaotic. In reality, however, with the application of RMP, there is no such thing as a sharp boundary separating the core region filled with nested flux surfaces from the edge region where field lines are chaotic. Between these two regions, there is an intermediate region, referred to as "critical chaos", in which structures like island chains and cantori (broken KAM surfaces) exist [34]. As island chains can degrade confinement and cantori can serve as effective barriers to field-line transport [35], these structures usually have non-negligible effects. To maintain the analytical tractability of our model, we suppose the field lines in the chaotic layer are truly chaotic and don't take the effects of island chains and cantori into consideration. The structure of our model can be summarized by the flowchart in figure 3. At the large-scale, a quasi-mode is driven by the magnetic curvature and the mean density gradient. When a background stochastic magnetic field is imposed, to maintain $\nabla \cdot \boldsymbol{J} = 0$, small-scale convective cells, also referred to as the microturbulence, are driven by the beat of the quasi-mode with the stochastic magnetic field. This microturbulence has a finite correlation with the magnetic perturbations, which can account for the reduced complexity observed in Choi's experiments. We can think of it as the suppression of the instability characteristic of a chaotic system by external noise [36]. The microturbulence further leads to the emergence of a turbulent viscosity and a turbulent diffusivity. The effects of the stochastic magnetic field on the quasi-mode are mainly reflected in three distinct ways: (1) stochastic magnetic fields can enhance the effective plasma inertia and reduce the effective drive, thus opposing the mode growth; (2) the turbulent viscosity and the turbulent diffusivity produced by the microturbulence can damp the quasi-mode by increasing mixing; (3) the microturbulence can react to the evolution of the quasi-mode, consequently leading to the formation of a feedback loop in the system. Though this reaction tends to destabilize the quasi-mode, its effect can be proved to be negligible as compared to (1). Combining (1), (2), and (3), the net effect of stochastic magnetic field on the quasi-mode is to slow the mode growth.

The remainder of this paper is organized as follows. In section 2, we briefly review the basics of the quasi-mode and demonstrate the resemblance between the quasi-mode and the ballooning mode. The model of the quasi-mode in an externally prescribed stochastic magnetic field is then formulated in section 3. Quantitative results, including the correction to the growth of the quasi-mode mode, the correlation $\langle \tilde{v}_x \tilde{\boldsymbol{b}} \rangle$, and the scaling of the turbulent viscosity ν_T, are also given in this section. In section 4, we pin down the sign of the growth rate correction and discuss its underlying physics. The consistency between our theory and existing simulations and experiments is also discussed there. This paper concludes with the lessons we have learned about the dynamics of the quasi-mode and what we can infer about the dynamics of the ballooning mode, and with suggestions for future experimental and theoretical investigations. Expressions for the operators in this work, as well as a detailed calculating procedure of the Jensen-Shannon complexity, are attached in the Appendix.

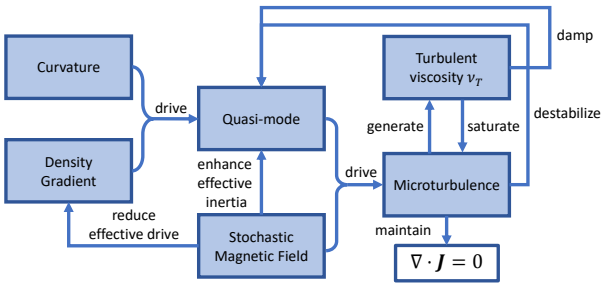

Figure 3. Multi-scale feedback loops of quasi-mode and small-scale convective cells.

2. Revisiting of the Quasi-mode

As mentioned in section 1, one challenge in studying the ballooning mode in a stochastic magnetic field is the difference in geometries upon which theories of the ballooning mode and resonant magnetic perturbations are based. The similarities between the quasi-mode and the ballooning mode allow us to study quasi-mode first and then extend the results to the ballooning mode. To elucidate the validity of this idea, fundamentals of the quasi-mode and the relation between the quasi-mode and the ballooning mode are discussed quantitatively in this section.

2.1. Physical picture of the quasi-mode

The quasi-mode was first identified by Roberts and Taylor in 1965 [37]. In a nutshell, a quasi-mode is an effective wave-packet of gravitational interchange modes in a sheared magnetic field, as depicted in figure 2. The term "quasi-mode" implies that it is not an eigenmode, so it will eventually disperse. But as will be discussed in section 2.3, the interchange modes constituting the quasi-mode are highly degenerate. So

the quasi-mode is capable of maintaining its shape before entering the nonlinear regime, and it is fair to treat quasi-mode as a "true mode". Unlike the gravitational interchange mode, which is localized at a specific horizontal surface, the convective cells of the quasi-mode (red envelopes in figure 2) have a broad mode structure in the x (vertical) direction. Since the main magnetic field has a small but finite shear, the fluid filaments or "flux tubes" (yellow columns in figure 2) must rotate around the vertical axis x when rising or falling. This rotation allows them to keep aligned with the local magnetic field so as to minimize the field distortion. Another name for the quasi mode, "twisted slicing mode", originates from this twisted interchange motion of the fluid filaments.

When the system is infinitely extended in the z direction, the quasi-mode, unlike gravitational interchange modes which are spatially periodic in z, exhibits a finite mode length in the direction of the main field. As illustrated in figure 4, the vertical and twisted sheets, filled alternately in red and blue, represent the envelope surfaces of the convective cells of the quasi-mode at various positions along the main field line. These convective cells correspond to the red envelope curves shown in figure 2. The colors red and blue represent the upward and downward motions of the plasma, respectively. The darker the shade, the faster the motion. From the change in color, it is evident that the plasma motion slows down (exponentially) as it moves away from the origin along the z axis. The length and direction of each arrow in figure 4 denote the magnitude and direction of the velocity field at the corresponding spatial position.

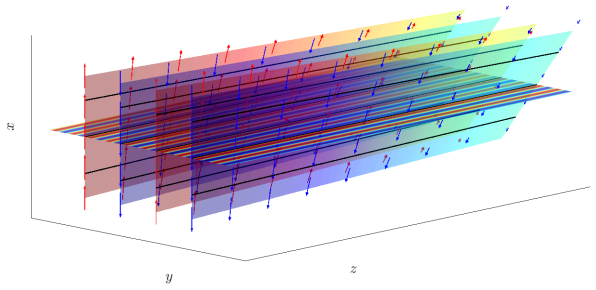

Figure 4. The velocity field of the quasi-mode and the graphic example of one of the magnetic perturbations. The vertical twisted sheets are envelope surfaces of the convective cells of the quasi-mode. The arrows are the visualization of the velocity field. The horizontal plane is a simple sketch of the magnetic perturbation at one particular resonant surface.

The finite mode length of the quasi-mode in the main field direction can be explained from the viewpoint of energy conservation. In the presence of magnetic shear, fluid filaments will rotate with respect to x axis as they move vertically. The rotational kinetic energy of these filaments would diverge if their mode length is equal to the length of the system (i.e., infinity). Hence, the mode length of the quasi-mode automatically adjusts to a finite value Δ. This adjustment is dictated by a balance among the rate of the release of the gravitational potential energy, the rate of the resistive dissipation, and the rate of the increase of the rotational kinetic energy. The underlying rationale is that to have a finite rotational kinetic energy, the quasi-mode must possess a finite length in z. This condition subsequently leads to an increase in the resistive dissipation. The increase in the rotational kinetic energy and dissipation is at the expense of the gravitational potential energy.

2.2. Quantitative description of the quasi-mode

The dynamics of both the gravitational interchange mode and the quasi-mode are governed by the same set of equations, i.e., resistive MHD equations. In this work, an incompressible plasma subject to a uniform gravitational field in the negative x direction is considered, as shown in figure 2. A uniform magnetic field B_0 is exerted in the z direction, along with a transverse field $B_y = sxB_0$, where s is a constant. The magnetic shear is assumed to be weak, i.e., $sx \ll 1$.

The linearized equations for the quasi-mode are the momentum equation, the induction equation, and the continuity equation

$$\rho_0 \frac{\partial \boldsymbol{v}}{\partial t} = -\nabla p + \frac{1}{4\pi}(\nabla \times \boldsymbol{B}) \times \boldsymbol{B_0} + \frac{1}{4\pi}(\nabla \times \boldsymbol{B_0}) \times \boldsymbol{B} + \rho \boldsymbol{g}, \tag{3}$$

$$\frac{\partial \boldsymbol{B}}{\partial t} = (\boldsymbol{B_0} \cdot \nabla)\, \boldsymbol{v} - (\boldsymbol{v} \cdot \nabla)\boldsymbol{B_0} + \frac{\eta}{4\pi}\nabla^2 \boldsymbol{B}, \tag{4}$$

$$\frac{\partial \rho}{\partial t} = -\boldsymbol{v} \cdot \nabla \rho_0 = -v_x \alpha \rho_0. \tag{5}$$

Note that the Ampère's law $\nabla \times \boldsymbol{B} = 4\pi \boldsymbol{J}$ is used to eliminate $\boldsymbol{J}$ in equation (3). In equations (3) through (5), $\boldsymbol{B_0} = (0, sx, 1)B_0$ is the main field. $\boldsymbol{g} = -g\hat{\boldsymbol{x}}$ is the "gravity", which can be identified in terms of the pressure p_0 and the magnetic curvature R_c by $g \sim 2p_0/\rho_0 R_c$. η is the plasma resistivity, which is assumed to be uniform in the system. α characterizes the gradient of the mean density, which acts as the source of free energy. In this case, ρ_0 increases linearly with x, so α is a constant. The Boussinesq approximation allow us to treat ρ_0 as uniform in equations (3) and (5). In equation (4), the ratio of $\partial_t \boldsymbol{B}$ to $\eta\nabla^2\boldsymbol{B}/4\pi$ is of order $\beta = 8\pi p_0/B_0^2$. In the limit of $\beta \ll 1$, we can eliminate the term $\partial_t \boldsymbol{B}$, leading to the equation

$$\boldsymbol{B_0} \cdot \nabla \boldsymbol{v} + \frac{\eta}{4\pi}\nabla^2 \boldsymbol{B} = 0, \tag{6}$$

where the term $\boldsymbol{v}\cdot\nabla\boldsymbol{B_0}$ is also disregarded due to the slow spatial variation of $\boldsymbol{B_0}$. Applying operator $(\nabla\times\nabla\times)$ to equation (3) yields

$$\rho_0\frac{\partial\nabla^2\boldsymbol{v}}{\partial t}=\frac{1}{4\pi}\boldsymbol{B}_0\cdot\nabla\left(\nabla^2\boldsymbol{B}\right)-\left[\nabla(\nabla\cdot\rho\boldsymbol{g})-\nabla^2\rho\boldsymbol{g}\right]. \quad (7)$$

Substituting equation (5) and (6) into equation (7) and taking the dot product with $\hat{\boldsymbol{x}}$, we obtain the following eigenmode equation

$$\rho_0\eta\frac{\partial^2\nabla^2 v_x}{\partial t^2}+\left(\boldsymbol{B}_0\cdot\nabla\right)^2\frac{\partial v_x}{\partial t}-\alpha g\rho_0\eta\left(\frac{\partial^2}{\partial y^2}+\frac{\partial^2}{\partial z^2}\right)v_x=0, \quad (8)$$

where $\boldsymbol{B_0}\cdot\nabla=B_0\left(\frac{\partial}{\partial z}+sx\frac{\partial}{\partial y}\right)$. In order to exploit the linear magnetic shear and simplify the operator $\boldsymbol{B_0}\cdot\nabla$, a twisted coordinate system, defined by the following transformation, is introduced:

$$\xi=x,\quad \chi=y-sxz,\quad \zeta=z. \quad (9)$$

The operators appearing in equation (8) also need to be transformed accordingly (see Appendix B). For the quasi-mode, instead of employing the Fourier expansion in the z direction, a more generalized form of the solutions is adopted, as shown below:

$$v_x=v(\zeta)\exp(\gamma_{\boldsymbol{k}}t+ik_x\xi+ik_y\chi). \quad (10)$$

Plugging equation (10) into equation (8), we get

$$\left(1+\epsilon^2 q\right)\frac{1}{k_y^2}\frac{\partial^2 v}{\partial\zeta^2}-\frac{2\epsilon^2 qis\xi}{k_y}\frac{\partial v}{\partial\zeta}-\epsilon^2\left[q\left(1+s^2\xi^2\right)+\frac{\gamma_{\boldsymbol{k}}^2}{\alpha g}s^2\zeta^2-\frac{\gamma_{\boldsymbol{k}}^2}{\alpha g}\left(\frac{k_x^2}{k_y^2}-2s\zeta\frac{k_x}{k_y}\right)\right]v=0, \quad (11)$$

where

$$\epsilon^2=\frac{\alpha g\rho_0\eta}{\gamma_{\boldsymbol{k}}B_0^2},\quad q=\frac{\gamma_{\boldsymbol{k}}^2}{\alpha g}-1. \quad (12)$$

In the regime where $\epsilon\ll 1$ (long mode length of the quasi-mode in the z direction), $k_x/k_y\ll 1$ (broad mode structure of the quasi-mode in the x direction), and $s\xi\ll 1$ (weak magnetic shear), equation (11) is simplified to

$$\frac{d^2v}{d\zeta^2}-\frac{\gamma_{\boldsymbol{k}}\tau_A}{S}\left(sk_y\right)^2\zeta^2 v+\frac{\gamma_{\boldsymbol{k}}\tau_A k_y^2}{S}\left(\frac{\alpha g}{\gamma_{\boldsymbol{k}}^2}-1\right)v=0, \quad (13)$$

where S is the Lundquist number defined as the ratio of the resistive diffusion time, $\tau_R=4\pi a/\eta$, to the Alfvén time, $\tau_A=a/(B_0/4\pi\rho_0)^{1/2}$. As equation (13) is similar in form to the equation for a quantum harmonic oscillator, its solutions are given by

$$v=v_j(\zeta)=2^{-\frac{j}{2}}H_j\left(\frac{\zeta}{\Delta}\right)\exp\left(-\frac{\zeta^2}{2\Delta^2}\right), \quad (14)$$

where H_j are the Hermite polynomials, Δ is the characteristic mode length along the main field. In the case of the slow interchange, i.e. $\gamma_{\boldsymbol{k}}^2\ll\alpha g$, the growth rate of this mode is

$$\gamma_{\boldsymbol{k}}^{(j)}=(\alpha g)^{\frac{2}{3}}\left(\frac{\tau_A k_y^2}{Ss^2}\right)^{\frac{1}{3}}(2j+1)^{-\frac{2}{3}}, \quad (15)$$

and the corresponding Δ is

$$\Delta_j=\frac{1}{(\alpha g)^{\frac{1}{6}}}\left(\frac{S}{\tau_A k_y^2}\right)^{\frac{1}{3}}\frac{1}{s^{\frac{1}{3}}}(2j+1)^{\frac{1}{6}}. \quad (16)$$

As the wavenumber k_x is irrelevant in equations (15) and (16) due to the fact that $k_x\ll k_y$, the x-dependence of the solutions can be replaced by any slowly varying function $g(x)$, leading to the solutions of equation (13) in the form of

$$v_x(x,y,z)=g(x)v_j(z)\exp\left[ik_y(y-sxz)\right]. \quad (17)$$

In section 3, *the function $g(x)$ is taken as a constant*, which is a reasonable approximation as long as we are not close to the system boundary.

2.3. Relation between quasi-mode and ballooning mode

The quasi-mode can be used as a surrogate for the ballooning mode because their share similar mode structures. More specifically, both of them are composed of localized modes. It can be shown that the expression for the quasi-mode given by equation (17) is just a linear superposition of the vertically localized gravitational interchange modes. Now we seek solutions of equation (8) that are periodic in z and of the form

$$v_x=v_g(x)\exp\left(\tilde{\gamma}_{\boldsymbol{k}}t+ik_y y+ik_z z\right). \quad (18)$$

By adopting this form and solving equation (8), the eigenmodes are given by

$$v_g(X)=u_j(X)=2^{-\frac{j}{2}}H_j\left(\frac{X}{\delta_{\boldsymbol{k}}}\right)\exp\left(-\frac{X^2}{2\delta_{\boldsymbol{k}}^2}\right), \quad (19)$$

with their growth rates in the slow interchange limit given as

$$\tilde{\gamma}_{\boldsymbol{k}}^{(j)}=(\alpha g)^{\frac{2}{3}}\left(\frac{\tau_A\tilde{k}^4}{Ss^2k_y^2}\right)^{\frac{1}{3}}(2j+1)^{-\frac{2}{3}}, \quad (20)$$

where

$$X=x+\frac{k_z}{sk_y},\quad \delta_{\boldsymbol{k}}=\left(\frac{\gamma_{\boldsymbol{k}}\tau_A}{Ss^2k_y^2}\right)^{\frac{1}{4}},\quad \tilde{k}^2=k_y^2+k_z^2. \quad (21)$$

These modes are localized around resonant surfaces where $\boldsymbol{k}\cdot\boldsymbol{B_0}=0$. For two modes with the same k_y but localized at different heights separated by x_0, their growth rates differs only by $\delta\gamma/\gamma\sim(sx_0)^2\ll 1$. The strong degeneracy of these localized gravitational interchange modes leads to a long "life-time" of the quasi-mode. Consequently, the sum of a series of interchange modes in the "ground state" ($j=0$), each

sharing the same k_y but centered at various resonant surfaces, can be written as

$$u(x,y,z,t) = \exp(ik_y y) \times \int f(k_z) \exp\left[ik_z z - \frac{(x-x_0)^2}{2\delta_0^2}\right] \exp(\gamma_{\boldsymbol{k}} t) dk_z, \quad (22)$$

where $f(k_z)$ is a slowly varying weight function, and $x_0 = -k_z/sk_y$. If we let $f(k_z)dk_z = -g(x_0)dx_0$, equation (22) reduces to

$$u(x,y,z,t) \cong \delta\sqrt{2}\pi g(x) \exp\left[ik_y(y - sxz) - \frac{(sk_y\delta_0 z)^2}{2} + \gamma t\right]. \quad (23)$$

The equivalence between equation (17) and equation (23) clearly exhibits the relation between the quasi-mode and the gravitational interchange mode. Note that $1/\Delta \cong sk_y\delta_{\boldsymbol{k}} \ll k_y$, suggesting that the narrower the interchange mode, the longer the quasi-mode.

Analogous to the quasi-mode, which acts as a wave-packet of the interchange modes, the ballooning mode is a coupling of poloidal harmonics localized at a sequence of resonant surfaces (see figure 2). There are two different but equivalent methods to investigate the "land of ballooning": ballooning mode representation [38] and Bloch eigenmode equation [39]. Here the former one is adopted to illuminate the similarity between the ballooning mode and the quasi-mode.

The most persistent instabilities in toroidal axisymmetric plasmas are those characterized by a short wavelength perpendicular to the magnetic field and a long wave lengths parallel to it, such as the ballooning mode. The ordinary representation of this kind of modes is in the eikonal form [40]

$$\varphi(r,\chi,\phi) = F(r,\chi) \exp\left[in(\phi - \int^{\chi} \nu d\chi)\right], \quad (24)$$

where χ is a poloidal, angle-like coordinate, $F(r,\chi)$ is a slowly varying function, ν is a parameter containing the information of magnetic geometry and related to the 'safety factor' by $q = 2\pi \oint \nu d\chi$. Note that the expression for the quasi-mode, given by equation (17), indeed takes this eikonal form. But in equation (17), the poloidal wavenumber k_y takes the place of the toroidal mode number n in equation (24). This is because in a torus, the toroidal symmetry is preserved whereas the poloidal symmetry is broken by the toroidicity effect. Hence, only the toroidal mode number n continues to be a valid "quantum" number. It can be proved that in the presence of magnetic shear, the eikonal form given by equation (24) contradicts with the demand of periodicity in the poloidal angle across all values of r, unless we assume $F(r,\chi)$ is not a slowly varying function. To reconcile this contradiction, in 1979, Connor, Hastie, and Taylor proposed the following ballooning mode transformation [38]

$$\varphi(r,\theta) = \sum_{m=-\infty}^{+\infty} e^{im\theta} \int_{-\infty}^{+\infty} e^{-im\eta} \hat{\varphi}(r,\eta) d\eta, \quad (25)$$

so that if $\hat{\varphi}(r,\eta)$ is a solution of

$$L(r,\eta)\hat{\varphi}(r,\eta) = \lambda\hat{\varphi}(r,\eta), \quad (26)$$

then $\varphi(r,\theta)$ will be a solution of

$$L(r,\theta)\varphi(r,\theta) = \lambda\varphi(r,\theta), \quad (27)$$

where $L(r,\theta)$ and $\varphi(r,\theta)$ are periodic in θ. This transformation effectively map the domain of $\theta \in (-\pi,\pi)$ onto the covering space of $\eta \in (-\infty,\infty)$, with η interpreted as the coordinate in the main field direction. After eliminating the periodicity requirement for $\hat{\varphi}$, it is feasible to express it in the eikonal form

$$\hat{\varphi}(r,\eta,\phi) = \varphi_0(r,\eta) \exp\left[-in(\phi - q\eta)\right], \quad (28)$$

where $\int^{\eta} \nu d\eta$ is approximated as $q\eta$ (i.e., the phase shift is neglected). Substituting equation (28) into equation (24), we obtain [41]

$$\varphi(r,\theta) = \sum_{m=-\infty}^{+\infty} \varphi_m(r, nq-m) e^{im\theta}, \quad (29)$$

where φ_m is defined as

$$\varphi_m(r, nq-m) = \int_{-\infty}^{+\infty} \frac{d\eta}{2\pi} \varphi_0(r,\eta) e^{i(nq-m)\eta}. \quad (30)$$

Since φ_0 is a slowly varying function of η, its Fourier transform φ_m is localized near the resonant surface where $q(r_{m,n}) = m/n$. Equation (29) indicates that a ballooning mode $\varphi(r,\theta)$ can be viewed as a coupling of a sequence of poloidal harmonics φ_m, as sketched in figure 2. This clearly demonstrates the resemblance between a quasi-mode wave-packet in a cylinder (or slab) and a ballooning mode in a torus. Therefore, by studying the quasi-mode in a stochastic magnetic field, we can provide instructive insights into the effects of stochastic magnetic field on ballooning mode.

3. Model Development

In this section, a multi-scale model for the quasi-mode in a stochastic magnetic field is presented. We show that the small-scale convective cells, i.e., the microturbulence, are driven when the stochastic magnetic field is introduced to the dynamics of the quasi-mode, so as to maintain $\nabla \cdot \boldsymbol{J} = 0$ at all scales. The correlation between the velocity fluctuations and the magnetic perturbations, the correction to the growth rate of the quasi-mode, and the scaling of the turbulent viscosity are also given.

3.1. Generation of the microturbulence

Compared to the eigenmode equation (8), the vorticity equation is better suited to demonstrate the generation of the microturbulence, as it is actually the equation $\nabla \cdot \boldsymbol{J} = 0$ in detail [42], and thus naturally guarantees quasi-neutrality. Taking the curl of the momentum equation (3), the vorticity equation is written as

$$\underbrace{-\frac{\rho_0}{B_0^2}\frac{\partial}{\partial t}\nabla_\perp^2\varphi}_{\nabla_\perp\cdot\boldsymbol{J_{pol}}}\underbrace{-\frac{1}{\eta}\left(\boldsymbol{b_0}\cdot\nabla\right)^2\varphi}_{\nabla_\parallel J_\parallel}+\underbrace{\frac{g}{B_0}\frac{\partial}{\partial y}\rho}_{\nabla_\perp\cdot\boldsymbol{J_{PS}}}=0, \tag{31}$$

where φ is the electrostatic potential. $J_\parallel$ is eliminated by exploiting the linearized Ohm's law [43]

$$J_\parallel=\frac{1}{\eta}\left(\boldsymbol{b_0}\cdot\nabla\right)\varphi=\frac{1}{4\pi}\left(\nabla\times\boldsymbol{B}\right)_\parallel, \tag{32}$$

in the $\beta \ll 1$ limit (electrostatic case). Combining it with the continuity equation (5), we get

$$\rho_0\eta\frac{\partial^2}{\partial t^2}\nabla_\perp^2\varphi+\frac{\partial}{\partial t}B_0^2\left(\boldsymbol{b_0}\cdot\nabla\right)^2\varphi-\alpha g\rho_0\eta\frac{\partial^2}{\partial y^2}\varphi=0. \tag{33}$$

Although there may appear to be a slight difference, equation (33) is, in fact, equivalent to equation (8), as

$$\begin{aligned}&\left|\frac{\rho_0\eta\partial_t^2\left(\boldsymbol{b_0}\cdot\nabla\right)^2\varphi}{\partial_t B_0^2\left(\boldsymbol{b_0}\cdot\nabla\right)^2\varphi}\right|=\frac{\rho_0\eta\gamma}{B_0^2}=\epsilon^2\frac{\gamma_{\boldsymbol{k}}^2}{\alpha g}\ll 1,\\&\left|\frac{\partial_z^2\varphi}{\partial_y^2\varphi}\right|\cong\left(s\delta\right)^2\ll 1.\end{aligned} \tag{34}$$

With the introduction of the magnetic perturbations, magnetic field lines become chaotic. Following a standard low-β, normal aspect ratio ordering, we have

$$\begin{aligned}&\tilde{b}_\perp=\tilde{B}_\perp/B_0\sim\epsilon,\quad \tilde{b}_\parallel=\tilde{B}_\parallel/B_0\sim\epsilon^2,\\&\nabla_\perp\sim 1,\quad \nabla_\parallel\sim\epsilon,\end{aligned} \tag{35}$$

where ϵ is a small number [44]. Then we introduce the stochastic magnetic potential $\tilde{A}$ and rewrite the perturbed magnetic as

$$\tilde{\boldsymbol{b}}=\tilde{\boldsymbol{B}}/B_0=\hat{\boldsymbol{z}}\times\nabla\tilde{A}+\tilde{b}_\parallel\hat{\boldsymbol{z}}, \tag{36}$$

whose divergence is then

$$\nabla\cdot\tilde{\boldsymbol{b}}=\partial_\parallel\tilde{b}_\parallel\sim\epsilon^3. \tag{37}$$

Hence, with the neglect of $\tilde{B}_\parallel$ and its effects, $\nabla\cdot\tilde{\boldsymbol{b}}=0$ remains accurate to the second order. Effects of $\tilde{B}_\parallel$ need to be reconsidered in the case of stochasticity in a spherical torus [45]. Then, the total magnetic field is approximated as the sum of a main field $\boldsymbol{B_0}$ and a perturbed field $\tilde{\boldsymbol{B}}_\perp$, i.e., $\boldsymbol{B_{tot}}=\boldsymbol{B_0}+\tilde{\boldsymbol{B}}_\perp$. Here $\tilde{\boldsymbol{B}}_\perp$ is constituted by a series of high-$\boldsymbol{k}$ magnetic perturbations that are highly localized at resonant surfaces and densely packed, i.e., $\sigma_{\text{Chirikov}}\gg 1$ (strong chaos). The horizontal plane in figure 4 depicts one such perturbation at a specific resonant surface. The stochastic magnetic field is incorporated into our model by modifying the parallel gradient operator to

$$\nabla_\parallel=\nabla_\parallel^{(0)}+\tilde{\boldsymbol{b}}\cdot\nabla_\perp, \tag{38}$$

where $\nabla_\parallel^{(0)}=\partial_\zeta$ is the gradient along the main field, $\tilde{\boldsymbol{b}}=\tilde{\boldsymbol{B}}_\perp/B_0$, and $\tilde{\boldsymbol{b}}\cdot\nabla_\perp$ is the gradient along the perturbed field. With this modification, the parallel current density becomes

$$\boldsymbol{J}_\parallel=-\frac{1}{\eta}\left[\nabla_\parallel^{(0)}+\tilde{\boldsymbol{b}}\cdot\nabla_\perp\right]\bar{\varphi}\left(\boldsymbol{b}_0+\tilde{\boldsymbol{b}}\right), \tag{39}$$

where $\bar{\varphi}$ denotes the electrostatic potential of the low $\boldsymbol{k}$ quasi-mode. Equation (39) implies that the plasma flow along the chaotic magnetic field lines results in a small-scale current density fluctuation $\tilde{\boldsymbol{J}}_\parallel$, whose divergence is

$$\nabla\cdot\tilde{\boldsymbol{J}}_\parallel=-\frac{1}{\eta}\left[\left(\tilde{\boldsymbol{b}}\cdot\nabla_\perp\right)\nabla_\parallel^{(0)}\bar{\varphi}+\nabla_\parallel^{(0)}\left(\tilde{\boldsymbol{b}}\cdot\nabla_\perp\right)\bar{\varphi}\right]. \tag{40}$$

Since the quasi-neutrality requires $\nabla\cdot\boldsymbol{J}=0$ at all scales, equation (40) is supposed to be equal to 0 if $\tilde{\boldsymbol{J}}_\parallel$ is the only contribution to the microscopic current. To verify this point, we take the Fourier expansion of $\tilde{\boldsymbol{b}}$ and $\bar{\varphi}$, yielding

$$\begin{aligned}\bar{\varphi}&=\bar{\varphi}_{\boldsymbol{k}}(\zeta)\exp\left[\gamma_{\boldsymbol{k}}t+ik_y\chi\right],\\\tilde{\boldsymbol{b}}&=\sum_{\boldsymbol{k_1}}\tilde{\boldsymbol{b}}_{\boldsymbol{k_1}}(x)\exp\left[i\left(k_{1y}y-k_{1z}z\right)\right]\\&=\sum_{\boldsymbol{k_1}}\tilde{\boldsymbol{b}}_{\boldsymbol{k_1}}\left(\hat{\xi}_{\boldsymbol{k_1}}\right)\exp\left[\left(ik_{1y}\chi+ik_{1\parallel}\zeta\right)\right],\end{aligned} \tag{41}$$

where $k_{1\parallel}=sk_{1y}\hat{\xi}_{\boldsymbol{k_1}}$, $\hat{\xi}_{\boldsymbol{k_1}}=\xi-\xi_{\boldsymbol{k_1}}$, $\xi_{\boldsymbol{k_1}}=k_{1z}/k_{1y}$. The twisted coordinate system (equation (9)) is employed here. As mentioned in section 2.2, the quasi-mode is assumed to be independent of ξ. Then by plugging equation (41) into equation (40), we have

$$\begin{aligned}&\left(\tilde{\boldsymbol{b}}\cdot\nabla_\perp\right)\nabla_\parallel^{(0)}\bar{\varphi}+\nabla_\parallel^{(0)}\left(\tilde{\boldsymbol{b}}\cdot\nabla_\perp\right)\bar{\varphi}\\&=\sum_{\boldsymbol{k_1}}\Bigg\{2ik_y\left[-s\zeta\tilde{b}_{x_{\boldsymbol{k_1}}}\left(\hat{\xi}_{\boldsymbol{k_1}}\right)+\tilde{b}_{y_{\boldsymbol{k_1}}}\left(\hat{\xi}_{\boldsymbol{k_1}}\right)\right]\frac{\partial\bar{\varphi}_{\boldsymbol{k}}(\zeta)}{\partial\zeta}\\&-sk_yk_{1y}\hat{\xi}_{\boldsymbol{k_1}}\left[-s\zeta\tilde{b}_{x_{\boldsymbol{k_1}}}\left(\hat{\xi}_{\boldsymbol{k_1}}\right)+\tilde{b}_{y_{\boldsymbol{k_1}}}\left(\hat{\xi}_{\boldsymbol{k_1}}\right)\right]\bar{\varphi}_{\boldsymbol{k}}(\zeta)\\&+ik_y\left[-s\tilde{b}_{x_{\boldsymbol{k_1}}}\left(\hat{\xi}_{\boldsymbol{k_1}}\right)\right]\bar{v}_{x\boldsymbol{k}}(\zeta)\Bigg\}\times\\&\exp\left[\gamma_{\boldsymbol{k}}t+i\left(k_{1y}+k_y\right)\chi+ik_{1\parallel}\zeta\right].\end{aligned} \tag{42}$$

To simplify equation (42), we consider the "ground state" of the quasi-mode given in equation (14) ($j=0$), and assume the stochastic magnetic potential $\tilde{A}$ has a Gaussian profile across the resonant surface, i.e.

$$\begin{aligned}&\bar{\varphi}_{\boldsymbol{k}}(\zeta)=\bar{\varphi}_0\exp\left(-\zeta^2/2\Delta^2\right),\\&\tilde{A}_{\boldsymbol{k_1}}\left(\hat{\xi}_{\boldsymbol{k_1}}\right)=\tilde{A}_{0\boldsymbol{k_1}}\exp\left(-\hat{\xi}_{\boldsymbol{k_1}}^2/2o_{\boldsymbol{k_1}}^2\right),\end{aligned} \tag{43}$$

where $o_{\boldsymbol{k_1}}$ is the island width. By integrating equation (43) into equation (42), we observe that for $\nabla\cdot\tilde{\boldsymbol{J}}=0$ to hold, the following equations

$$\left(2\frac{\zeta^2}{\Delta^2}-1\right)+\frac{\xi_{\boldsymbol{k_1}}^2}{o_{\boldsymbol{k_1}}^2}=0,\quad \frac{2}{\Delta^2 o_{\boldsymbol{k_1}}^2}-s^2k_{1y}^2=0 \tag{44}$$

must be satisfied for arbitrary $\boldsymbol{k_1}$, which is clearly impossible. This brings us back to the narrative we developed in our previous study on resistive interchange modes in a stochastic magnetic field [10], i.e., small-scale convective cells must be driven by the beat of stochastic magnetic field with quasi-mode, which further generate a current density fluctuation $\tilde{\boldsymbol{J}}_\perp$ so as to keep $\nabla\cdot(\tilde{\boldsymbol{J}}_\parallel+\tilde{\boldsymbol{J}}_\perp)=0$. Figure 5 provides a heuristic illustration of the physical mechanism underpinning the formation of small-scale convective cells. According to the continuity equation of charge, $\nabla\cdot\tilde{\boldsymbol{J}}_\parallel\neq 0$ implies the accumulation of the polarization charge. Consider the term $\nabla_\parallel^{(0)}\left(\tilde{b}_y\partial_y\bar{\varphi}\right)$ on the R.H.S of equation (40) as an example, which actually serves as the main drive of the small-scale convective cells. With the profiles provided in equation (43), it turns out that this term leads to a polarization charge fluctuation, whose profile across the resonant surface is proportional to $\xi_{\boldsymbol{k_1}}^2/o_{\boldsymbol{k_1}}^2\exp(-\xi_{\boldsymbol{k_1}}^2/2o_{\boldsymbol{k_1}}^2)$. This accumulation of polarization charge is responsible for the emergence of the electrostatic potential fluctuation $\tilde{\varphi}$ and the resulting convective cells $\tilde{v}_{x_{\boldsymbol{k_1}}}$, as sketched by the purple dotted line in figure 5. Since the generation of small-scale convective cells is an outcome of the introduction of $\tilde{\boldsymbol{b}}$, it's to be expected that there exists a non-trivial correlation $\langle\tilde{\boldsymbol{b}}\tilde{v}_x\rangle$. This correlation is further calculated in section 3.3.

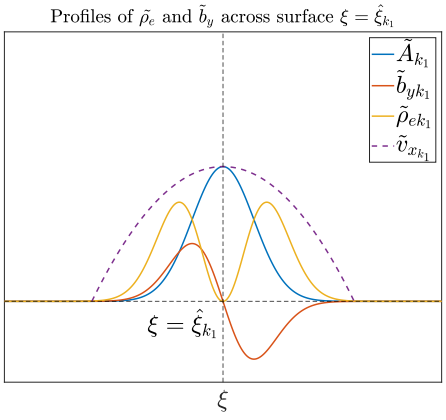

Figure 5. The profiles of $\tilde{A}_{\boldsymbol{k_1}}$, $\tilde{b}_{y_{\boldsymbol{k_1}}}$, $\tilde{\rho}_{e_{\boldsymbol{k_1}}}$ and $\tilde{v}_{x_{\boldsymbol{k_1}}}$ across the resonant surface $\xi=\xi_{\boldsymbol{k_1}}$. The stochastic magnetic field gives rise to the polarization charge fluctuation, which further induces a velocity fluctuation. Obviously, there is a non-zero correlation between $\tilde{A}$ and $\tilde{v}_x$.

3.2. Formulation of a multi-scale system

As depicted in figure 6, a large-scale quasi-mode, a background stochastic magnetic field, and the microturbulence are the three main "players" in our model. Hence, the vorticity equation and the

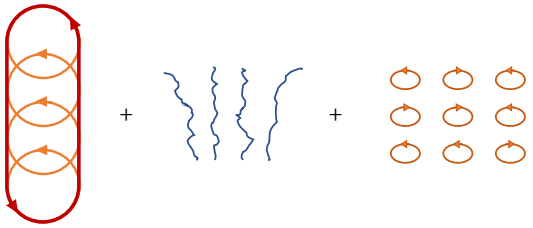

Figure 6. A sketch of the multi-scale model in this work: a large-scale quasi-mode (red envelope curves), a small-scale background stochastic magnetic field (blue curves), and small-scale convective cells (orange cells).

continuity equation are modified to

$$\left(\frac{\partial}{\partial t}-\nu_T\nabla_\perp^2\right)\nabla_\perp^2(\bar{\varphi}+\tilde{\varphi})+ \frac{S}{\tau_A}\left(\frac{\partial}{\partial\zeta}+\tilde{\boldsymbol{b}}\cdot\nabla_\perp\right)^2(\bar{\varphi}+\tilde{\varphi})-\frac{gB_0}{\rho_0}\frac{\partial(\bar{\rho}+\tilde{\rho})}{\partial y}=0, \tag{45}$$

and

$$\left(\frac{\partial}{\partial t}-D_T\nabla_\perp^2\right)(\bar{\rho}+\tilde{\rho})=-(\bar{v}_x+\tilde{v}_x)\,\alpha\rho_0. \tag{46}$$

Here $\bar{\rho}$, $\bar{\varphi}$, and $\bar{\boldsymbol{v}}$ are the plasma mass density, electrostatic potential, and resultant $E\times B$ drift velocity fluctuations of the quasi-mode, $\tilde{\rho}$, $\tilde{\varphi}$ and $\tilde{\boldsymbol{v}}$ are the density, electrostatic potential and resultant $E\times B$ drift velocity fluctuations of the microturbulence. The expressions for the operators in equation (45) and (46) are given by equation (B.2) in Appendix B. With the emergence of the small-scale convective cells, the time derivative ∂_t in equation (5) and (31) should be modified to $\partial_t+\tilde{\boldsymbol{v}}\cdot\nabla$ to account for the random advection of the quasi-mode by small-scale convective cells. This random advection $\tilde{\boldsymbol{v}}\cdot\nabla$ can be renormalized as a diffusion operator $-\nu_T\nabla_\perp^2$ or $-D_T\nabla_\perp^2$ [46]. The turbulent viscosity ν_T and the turbulent diffusivity D_T thus enter our model. In this work, the Schmidt number Sc is set to 1, i.e., $\nu_T=D_T$, as their physical mechanisms are the same.

In both section 2 and the prior work, the slow interchange approximation is utilized for the large-scale resistive interchange mode and the quasi-mode. So for consistency and simplicity, the same setup is adopted in our model, namely $k_y\ll 1/\delta_{\boldsymbol{k}}$, where $\delta_{\boldsymbol{k}}$ is the width of the localized interchange mode defined in equation (21). Owing to the small spatial scales of $\tilde{\boldsymbol{b}}$ and the fact that $\tilde{\boldsymbol{v}}$ emerges as a response to $\tilde{\boldsymbol{b}}$, $\tilde{\boldsymbol{v}}$ also exhibits small

spatial scales. More specifically, as the wavenumbers of $\tilde{\boldsymbol{b}}$ and $\tilde{\boldsymbol{v}}$ in the y direction are very large, it is reasonable to posit that those small-scale convective cells are fast interchange. It means $k_{1y} \gg 1/\delta_{\boldsymbol{k_1}}$, where $\delta_{\boldsymbol{k_1}}$ is the characteristic width of $\tilde{\boldsymbol{v}}_{\boldsymbol{k_1}}$. In addition, based on the definition, $1/\Delta \cong sk_y\delta_{\boldsymbol{k}} \ll sk_{1y}\delta_{\boldsymbol{k_1}} \cong k_{1\parallel}$. And by requiring the magnitudes of $\tilde{b}_x$ and $\tilde{b}_y$ are of the same order, it follows that $k_{1y} \cong o_{\boldsymbol{k_1}}$. According to the above discussion, the spatial ordering of our system is

$$\begin{aligned}\underbrace{\left|\frac{1}{\bar{\varphi}}\frac{\partial\bar{\varphi}}{\partial\xi}\right|}_{=0} &\ll \left|\frac{1}{\bar{\varphi}}\frac{\partial\bar{\varphi}}{\partial\zeta}\right| \ll \left|\frac{1}{\bar{\varphi}}\frac{\partial\bar{\varphi}}{\partial\chi}\right| \\ &\ll \left|\frac{1}{\tilde{\varphi}}\frac{\partial\tilde{\varphi}}{\partial x}\right| \ll \left|\frac{1}{\tilde{\varphi}}\frac{\partial\tilde{\varphi}}{\partial\chi}\right|, \\ \left|\frac{1}{\bar{\varphi}}\frac{\partial}{\partial\zeta}\bar{\varphi}\right| &\ll \left|\frac{1}{\tilde{\varphi}}\frac{\partial}{\partial\zeta}\tilde{\varphi}\right| \ll \left|\frac{1}{\tilde{\varphi}}\frac{\partial}{\partial\chi}\tilde{\varphi}\right|.\end{aligned} \tag{47}$$

In our prior work, it was highlighted that the growth of small-scale convective cells, recognized as fast interchange, is over-saturated by ν_T and D_T. This implies that the fast interchange growth rate $\gamma_{\boldsymbol{k_1}} = (\alpha g)^{1/2}$, is smaller than the turbulent damping rates $\nu_T k_{1y}^2$. In contrast, due to the small magnitude of the magnetic perturbation, we can treat its effect on the quasi-mode as a perturbation, and thus have $\nu_T k_y^2 \ll \gamma_{\boldsymbol{k}}$. Then the temporal ordering of our model is

$$\nu_T k_y^2 \ll \gamma_{\boldsymbol{k}} \ll \gamma_{\boldsymbol{k}_1} < \nu_T k_{1y}^2. \tag{48}$$

Inequalities (47) and (48) indicate a separation of the spatio-temporal scales in this model. For such as multi-scale system, we can employ the method of averaging to separate the dynamics of different scales. By adopting the spatial averaging defined as

$$\langle A\rangle = \bar{A} = \frac{1}{L_y}\int_{-L_y/2}^{L_y/2} e^{-ik_y\chi} A d\chi, \tag{49}$$

where χ is the coordinate defined in equation (9), the full set of equations for this model is given as follows:

$$\begin{aligned}&\left(\frac{\partial}{\partial t} - \nu_T\nabla_\perp^2\right)\nabla_\perp^2\bar{\varphi} + \frac{S}{\tau_A}\frac{\partial^2}{\partial\zeta^2}\bar{\varphi} \\ &+\frac{B_0^2}{\eta}\left\{\underbrace{\left\langle\left(\tilde{\boldsymbol{b}}\cdot\nabla_\perp\right)^2\right\rangle}_{(a)}\bar{\varphi} + \underbrace{\left\langle\frac{\partial}{\partial\zeta}\left(\tilde{\boldsymbol{b}}\cdot\nabla_\perp\right)\tilde{\varphi}\right\rangle}_{(b)}\right. \\ &\left.+\underbrace{\left\langle\left(\tilde{\boldsymbol{b}}\cdot\nabla_\perp\right)\frac{\partial}{\partial\zeta}\tilde{\varphi}\right\rangle}_{(c)}\right\} - \frac{gB_0}{\rho_0}\frac{\partial}{\partial y}\bar{\rho} = 0,\end{aligned} \tag{50a}$$

$$\left(\frac{\partial}{\partial t} - \nu_T\nabla_\perp^2\right)\nabla_\perp^2\tilde{\varphi} + \frac{S}{\tau_A}\frac{\partial^2}{\partial\zeta^2}\tilde{\varphi} + \frac{S}{\tau_A}\left\{\frac{\partial}{\partial\zeta}\left(\tilde{\boldsymbol{b}}\cdot\nabla_\perp\right)\bar{\varphi} + \left(\tilde{\boldsymbol{b}}\cdot\nabla_\perp\right)\frac{\partial}{\partial\zeta}\bar{\varphi}\right\}$$

$$-\frac{gB_0}{\rho_0}\frac{\partial}{\partial y}\tilde{\rho} = 0, \tag{50b}$$

$$\left(\frac{\partial}{\partial t} - D_T\nabla_\perp^2\right)\bar{\rho} = -\bar{v}_x\alpha\rho_0, \tag{50c}$$

$$\left(\frac{\partial}{\partial t} - D_T\nabla_\perp^2\right)\tilde{\rho} = -\tilde{v}_x\alpha\rho_0. \tag{50d}$$

As can be seen from these equations, dynamics of the large-scale quasi-mode and the small-scale convective cells are coupled to each other. On the one hand, terms involving the beat of $\tilde{\boldsymbol{b}}$ and $\bar{\varphi}$ act as the source of equation (50b), driving the microturbulence $\tilde{\varphi}$. On the other hand, in equation (50a), terms involving $\tilde{\varphi}$ can react on the evolution of the quasi-mode $\bar{\varphi}$.

The workflow of the remaining calculations in this paper can be summarized by figure 7. After using the method of averaging to separate the dynamics at different scales, the next step is to get the linear response of $\tilde{v}_x$ to the beat of $\tilde{\boldsymbol{b}}$ with $\bar{v}_x$ by solving the small-scale dynamics. The correlation between $\tilde{v}_x$ and $\tilde{\boldsymbol{b}}$ is calculated by exploiting this linear response. Then, upon plugging the linear response into equation (50a), the revised eigenmode equation for the quasi-mode, which includes all the effects of the stochastic magnetic field, is obtained. Subsequently, the corrected growth rate of the quasi-mode is computed via perturbation theory. Finally, a simple nonlinear closure model is used to compute the scaling of the turbulent viscosity and the turbulent diffusivity arising from the microturbulence.

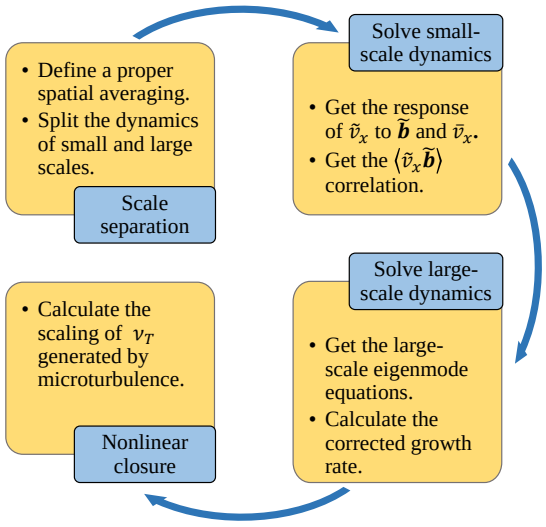

Figure 7. The workflow of the remaining calculation.

3.3. Correlation between $\tilde{v}_x$ and $\tilde{\boldsymbol{b}}$

To determine the effect of the stochastic magnetic field on the growth rate of the quasi-mode, the unknown

quantity, $\tilde{\varphi}$, must be eliminated from equation (50a). This requires us to find the response of $\tilde{\varphi}$ to $\tilde{\boldsymbol{b}}$, which can be obtained from equation (50b). Similar to the Fourier series of $\tilde{\boldsymbol{b}}$ given in equation (41), the Fourier series of $\tilde{\varphi}$ and $\tilde{\rho}$ are

$$\begin{aligned}\tilde{\varphi} &= \sum_{\boldsymbol{k_1}} \tilde{\varphi}_{\boldsymbol{k_1}}\left(\hat{\xi}_{\boldsymbol{k_1}},\zeta\right)\exp\left[\gamma_{\boldsymbol{k}}t + ik_{1y}\chi + ik_{1\parallel}\zeta\right],\\ \tilde{\rho} &= \sum_{\boldsymbol{k_1}} \tilde{\rho}_{\boldsymbol{k_1}}\left(\hat{\xi}_{\boldsymbol{k_1}},\zeta\right)\exp\left[\gamma_{\boldsymbol{k}}t + ik_{1y}\chi + ik_{1\parallel}\zeta\right],\end{aligned} \tag{51}$$

where $\tilde{\varphi}_{\boldsymbol{k_1}}$ and $\tilde{\rho}_{\boldsymbol{k_1}}$ are slowly varying functions of ζ. Note that the growth rates of $\tilde{\varphi}$ and $\tilde{\rho}$ are the slow interchange growth rate $\gamma_{\boldsymbol{k}}$, rather than the fast interchange growth rate $\gamma_{\boldsymbol{k_1}}$. This is because the growth of $\tilde{\varphi}$ and $\tilde{\rho}$ is over-saturated by the turbulent viscosity ν_T and the turbulent diffusivity D_T, and adiabatically modulated by the growth of the quasi-mode. As a result, both sides of equation (50b) grow at the same rate.

Since the quasi-mode is not periodic in the main field direction, it is challenging to define an appropriate averaging over ζ. Therefore, the spatial averaging employed in this work, as defined by equation (49), differs from the one used for the resistive interchange mode. In our previous work, the averaging was carried out in both toroidal and poloidal directions. While this averaging scheme is able to separate the dynamics of large and small scales, it only provides the relation between a spectrum of $\tilde{\varphi}_{\boldsymbol{k_1}}$ with the same k_{1y} and a spectrum of $\tilde{\boldsymbol{b}}_{\boldsymbol{k_2}}$ with the same k_{2y}, rather than the response of a single $\tilde{\varphi}_{\boldsymbol{k_1}}$ to a single $\tilde{\boldsymbol{b}}_{\boldsymbol{k_2}}$. To address this issue, we suppose that only magnetic perturbations $\tilde{\boldsymbol{b}}_{\boldsymbol{k_2}}$ that are located at the same resonance surface as $\tilde{\varphi}_{\boldsymbol{k_1}}$ can drive $\tilde{\varphi}_{\boldsymbol{k_1}}$. In other words, only the *coherent response* of $\tilde{\varphi}_{\boldsymbol{k1}}$ to $\tilde{\boldsymbol{b}}_{\boldsymbol{k2}}$ is considered. Since both of $\tilde{\varphi}_{\boldsymbol{k_1}}$ and $\tilde{\boldsymbol{b}}_{\boldsymbol{k_2}}$ are highly localized near the resonant surfaces, this is a fair assumption. Substituting equation (50d) and (51) into equation (50b), and simplifying it according to the scale orderings given by inequalities (47) and (48), we get

$$\begin{aligned}&-2\nu_T k_{1y}^2\frac{\partial^2}{\partial\xi^2}\tilde{v}_{x\boldsymbol{k_1}} + \frac{S}{\tau_A}s^2k_{1y}^2\hat{\xi}_{\boldsymbol{k_1}}^2\tilde{v}_{x\boldsymbol{k_1}}\\ &\quad-\left(\frac{\alpha g}{D_T}-\nu_T k_{1y}^4\right)\tilde{v}_{x\boldsymbol{k_1}}\\ &\quad=\frac{S}{\tau_A}ik_{1y}\left[-s\tilde{b}_{\boldsymbol{k_2}}\left(2\zeta\partial_\zeta+1\right)+2\tilde{b}_{y_{\boldsymbol{k_2}}}\partial_\zeta\right]\bar{v}_{x\boldsymbol{k}}\\ &\quad-\frac{S}{\tau_A}k_{1y}k_{2\parallel}\left[-s\zeta\tilde{b}_{x_{\boldsymbol{k_2}}}+\tilde{b}_{y_{\boldsymbol{k_2}}}\right]\bar{v}_{x\boldsymbol{k}},\end{aligned} \tag{52}$$

where $\tilde{v}_{x\boldsymbol{k_1}} = -ik_{1y}\tilde{\varphi}_{\boldsymbol{k_1}}/B_0$, $\bar{v}_{x\boldsymbol{k}} = -ik_y\bar{\varphi}_{\boldsymbol{k}}/B_0$, and $\boldsymbol{k_1}$ and $\boldsymbol{k_2}$ satisfy relations

$$k_{1y} = k_{2y} + k_y, \quad \frac{k_{2z}}{sk_{2y}} = \frac{k_{1z}}{sk_{1y}}. \tag{53}$$

The extra Fourier factor $\exp(-isk_y\zeta\hat{\xi}_{\boldsymbol{k_1}})$ on the R.H.S is set to unity as the scale $sk_y\zeta \sim sk_y\Delta \sim 1/\delta_{\boldsymbol{k}}$ is irrelevant to the small-scale dynamics. It is more straightforward to see the significance of the drive by the beat of $\tilde{\boldsymbol{b}}$ and $\bar{v}_x$ from equation (52). If we retain the temporal variation of $\tilde{v}_{x\boldsymbol{k_1}}$, divide it by k_{1y}^2, and exploit the spatial-temporal ordering given by inequalities (47) and (48), equation (52) can be rewritten into the following heuristic form

$$\frac{\partial}{\partial t}\tilde{v}_{x\boldsymbol{k_1}} + \lambda\tilde{v}_{x\boldsymbol{k_1}} = \hat{D}\left[\tilde{\boldsymbol{b}}\bar{v}_x\right], \tag{54}$$

where

$$\lambda = \nu_T k_{1y}^2 - \frac{\alpha g}{D_T k_{1y}^2} \approx \nu_T k_{1y}^2 - (\alpha g)^{1/2}, \tag{55}$$

$\hat{D}$ denotes the drive by $\tilde{\boldsymbol{b}}\bar{v}_x$ beats on the R.H.S of equation (52). The first term in the expression for λ represents the turbulent damping, and the second term is the linear drive by the mean density gradient. As small-scale convective cells grow fast under the drive of mean density gradient, the nonlinear effect, i.e., the renormalized turbulent viscosity, will also increase so that at a point ν_T becomes large enough to over-saturate the linear drive, i.e., $\lambda > 0$. The processes of the linear growth and the over-saturation of $\tilde{v}_{x\boldsymbol{k}}$ both happen on a very short time scale $\sim \mathcal{O}(1/\gamma_{\boldsymbol{k_1}})$. On the longer time scale $\sim \mathcal{O}(1/\gamma_{\boldsymbol{k}})$, as the quasi-mode $\bar{v}_{x\boldsymbol{k}}$ varies with time, the drive $\hat{D}$ on the R.H.S of equation (54) will modulate the microturbulence $\tilde{v}_{x\boldsymbol{k_1}}$ adiabatically. One may notice that equation (54) is similar in structure to a Langevin equation, which further suggests a fluctuation-dissipation balance. The stochastic magnetic field $\tilde{\boldsymbol{b}}$ thus has dual identities: on the one hand, it serves as the drive (recall the random kicks in Brownian motion) to excite the microturbulence; on the other hand, the turbulence viscosity arising from $\tilde{\boldsymbol{b}}$ damps the growth of the small-scale convective cell, akin to the drag term in the Langevin equation.

Observing that the L.H.S of equation (52) is homogeneous in $\tilde{\varphi}_{\boldsymbol{k_1}}$ and resembles the equation for the quantum harmonic oscillator, the corresponding Green's function of equation (52) is [47]

$$G\left(\hat{\xi}_{\boldsymbol{k_1}},\hat{\xi}'_{\boldsymbol{k_1}}\right) = \sum_l \frac{\psi^l_{\boldsymbol{k_1}}\left(\hat{\xi}_{\boldsymbol{k_1}}\right)\psi^l_{\boldsymbol{k_1}}\left(\hat{\xi}'_{\boldsymbol{k_1}}\right)}{\Lambda^l_{\boldsymbol{k_1}} - \Lambda_{\boldsymbol{k_1}}}, \tag{56}$$

where

$$\begin{aligned}&\psi^l_{\boldsymbol{k_1}}(\hat{\xi}_{\boldsymbol{k_1}}) = \frac{H_l\left(\frac{\hat{\xi}_{\boldsymbol{k_1}}}{w'}\right)}{\pi^{\frac{1}{4}}w'^{\frac{1}{2}}\sqrt{2^l l!}}\exp\left[-\frac{1}{2}\left(\frac{\hat{\xi}_{\boldsymbol{k_1}}}{w'}\right)^2\right],\\ &{\Lambda_{\boldsymbol{k_1}}\boldsymbol{k_1}}^l = \frac{4\rho_0\nu_T k_{1y}^2}{w'^2}\left(l+\frac{1}{2}\right) \ll \Lambda_{\boldsymbol{k_1}} = -\rho_0\nu_T k_{1y}^4,\\ &w' = w_{\boldsymbol{k_1}} = \left(\frac{2\tau_A\nu_T}{Ss^2}\right)^{\frac{1}{4}}.\end{aligned} \tag{57}$$

Note that $w_{\boldsymbol{k_1}}/\delta_{\boldsymbol{k_1}} = (2\nu_T k_{1y}^2/\gamma_{\boldsymbol{k_1}})^{1/4} > 1$, which indicates the turbulent viscosity can broaden the width

of $\tilde{\varphi}_{\boldsymbol{k_1}}$. But as $w_{\boldsymbol{k_1}}/\delta_{\boldsymbol{k}} = (\nu_T k_y^2/\gamma_{\boldsymbol{k}})^{1/4} < 1$, the spatial ordering given by equation (47) remains valid. Utilizing this Green's function, we obtain the approximate solution of equation (52) given as follows

$$\begin{aligned}
&\tilde{v}_{x\boldsymbol{k_1}} \approx \tilde{v}^{(l=0)}_{x\boldsymbol{k_1}} + \tilde{v}^{(l=1)}_{x\boldsymbol{k_1}},\\
&\tilde{v}^{(l=0)}_{x\boldsymbol{k_1}} \approx \frac{S}{\tau_A \nu_T k_{1y}^4} \frac{\sqrt{2} o_{\boldsymbol{k_2}} \tilde{A}_{0\boldsymbol{k_2}}}{w'}\\
&[-2sk_{1y}k_{2y}\zeta\partial_\zeta \bar{v}_{x\boldsymbol{k}}(\zeta)] \exp\left[-\frac{1}{2}\left(\hat{\xi}_{\boldsymbol{k_1}}/w'\right)^2\right],\\
&\tilde{v}^{(l=1)}_{x\boldsymbol{k_1}} \approx -\frac{S}{\tau_A \nu_T k_{1y}^4} \frac{\sqrt{2} o_{\boldsymbol{k_2}} \tilde{A}_{0\boldsymbol{k_2}}}{w'} [2ik_{1y}\partial_\zeta \bar{v}_{x\boldsymbol{k}}(\zeta)\\
&+is^2 k_{1y} k_{2y}^2 o_{\boldsymbol{k_2}}^2 \zeta \bar{v}_{x\boldsymbol{k}}(\zeta)] \frac{2x}{w'} \exp\left[-\frac{1}{2}\left(\hat{\xi}_{\boldsymbol{k_1}}/w'\right)^2\right].
\end{aligned} \tag{58}$$

Without loss of physics and for simplicity, only the first two terms of the Green's function (i.e., $l = 0$ and $l = 1$ terms) are retained, representing the even and odd parity of the solution, respectively. With this solution, the correlation between $\tilde{v}_x$ and $\tilde{\boldsymbol{b}}$, which is a function of ζ, can be expressed as

$$\begin{aligned}
&\langle \tilde{v}_x \tilde{b}_x \rangle = \sum_{\boldsymbol{k_1}} \tilde{v}_{x(\boldsymbol{k}-\boldsymbol{k_1})} \tilde{b}_{x\boldsymbol{k_1}}\\
&= \frac{iL_yL_z}{(2\pi)^2} \int dk_{1y} \frac{s^2 k_y S \left|\tilde{A}_{0\boldsymbol{k_1}}\right|^2}{\tau_A \nu_T |k_{1y}|} \frac{12\sqrt{\pi} o_{\boldsymbol{k_1}}^2}{w'} \zeta \partial_\zeta \bar{v}_{x\boldsymbol{k}},\\
&\langle \tilde{v}_x \tilde{b}_y \rangle = \sum_{\boldsymbol{k_1}} \tilde{v}_{x(\boldsymbol{k}-\boldsymbol{k_1})} \tilde{b}_{y\boldsymbol{k_1}}\\
&= -\frac{iL_yL_z}{(2\pi)^2} \int dk_{1y} \frac{s^3 k_y S \left|\tilde{A}_{0\boldsymbol{k_1}}\right|^2}{\tau_A \nu_T |k_{1y}|} \frac{12\sqrt{\pi} o_{\boldsymbol{k_1}}^4}{w'^3} \zeta \bar{v}_{x\boldsymbol{k}},
\end{aligned} \tag{59}$$

where the summation over $\boldsymbol{k_1}$ is transformed into an integral over k_{1y} and $\xi_{\boldsymbol{k_1}}$, i.e.

$$\sum_{\boldsymbol{k_1}} = \frac{L_zL_y}{(2\pi)^2} \int dk_{1y} s\,|k_{1y}| \int d\xi_{\boldsymbol{k_1}}. \tag{60}$$

This is a fair transformation as magnetic perturbations $\tilde{\boldsymbol{b}}_{\boldsymbol{k_1}}$ at different resonant surfaces are densely packed.

The non-trivial correlation between $\tilde{v}_x$ and $\tilde{\boldsymbol{b}}$ given in equation (59) could serve as a cause for the reduction in the Jensen-Shannon complexity of the edge turbulence during the RMP ELM suppression phase. $\langle \tilde{v}_x \tilde{\boldsymbol{b}} \rangle \neq 0$ means that when RMP is applied, high-$\boldsymbol{k}$ fluctuations are generated and coupled to the stochastic magnetic field. In other words, the microturbulence "locks on" to the ambient stochasticity, and thus the statistical characteristics of the edge turbulence are changed by the externally prescribed magnetic perturbations. As mentioned in section 1, noisy signals have lower complexity. If we think of the magnetic perturbations as external noise, then the non-trivial correlation $\langle \tilde{v}_x \tilde{\boldsymbol{b}} \rangle$ makes statistics of edge turbulence more akin to those of noise, which is manifested as the reduction in its complexity in experiments. This can be interpreted as the suppression of the instability characteristic of a chaotic system by external noise [36]. Of course, we acknowledge that stochastic magnetic fields are not noise in the strict sense, but rather deterministic chaos. The effects of the stochastic magnetic field on the statistics of edge turbulence indeed provides a possible explanation for the experimental phenomena. A deeper approach for further justification for our claim would be to study the changes in complexity when two chaotic systems are superposed. This will be discussed in more detail in section 4.3 as a direction for future study.

3.4. Correction to the quasi-mode growth rate and scaling of the turbulent viscosity

Using the spatial averaging defined by equation (49), the Fourier series of $\tilde{\boldsymbol{b}}$ and $\tilde{\varphi}$ given in equation (41) and (51), the response of $\tilde{v}_x$ to $\tilde{\boldsymbol{b}}$ given in equation (58), and replacing the summation over $\boldsymbol{k_1}$ by integral, the three correlations in equation (50a) are equal to

$$\begin{aligned}
(a) &= \left\langle \left(\tilde{\boldsymbol{b}} \cdot \nabla_\perp\right)^2 \right\rangle \bar{\varphi}\\
&= \left[-s^2\zeta^2 k_y^2 \left|\tilde{b}_x^2\right| + 2s\zeta k_y^2 \left|\tilde{b}_x \tilde{b}_y\right| - k_y^2 \left|\tilde{b}_y^2\right|\right] \bar{\varphi}_{xk},
\end{aligned} \tag{61}$$

$$\begin{aligned}
&(b) + (c)\\
&= \left\langle \partial_\zeta \left(\tilde{\boldsymbol{b}} \cdot \nabla_\perp\right) \tilde{\varphi} + \left(\tilde{\boldsymbol{b}} \cdot \nabla_\perp\right) \partial_\zeta \tilde{\varphi} \right\rangle^{(l=0)}\\
&+ \left\langle \partial_\zeta \left(\tilde{\boldsymbol{b}} \cdot \nabla_\perp\right) \tilde{\varphi} + \left(\tilde{\boldsymbol{b}} \cdot \nabla_\perp\right) \partial_\zeta \tilde{\varphi} \right\rangle^{(l=1)},
\end{aligned}$$

$$\begin{aligned}
&\left\langle \partial_\zeta \left(\tilde{\boldsymbol{b}} \cdot \nabla_\perp\right) \tilde{\varphi} + \left(\tilde{\boldsymbol{b}} \cdot \nabla_\perp\right) \partial_\zeta \tilde{\varphi} \right\rangle^{(l=0)}\\
&\approx -\frac{L_zL_y}{(2\pi)^2} \int dk_{1y} \left\{ \frac{Ss^3 k_y^2 \left|\tilde{A}_{0\boldsymbol{k_1}}\right|^2}{\tau_A \nu_T |k_{1y}|} \times \right.\\
&\left. \frac{8\sqrt{\pi}\,|o_{\boldsymbol{k_1}}|^2}{w'} \right\} \zeta \partial_\zeta \bar{\varphi}_{\boldsymbol{k}},
\end{aligned} \tag{62}$$

$$\begin{aligned}
&\left\langle \partial_\zeta \left(\tilde{\boldsymbol{b}} \cdot \nabla_\perp\right) \tilde{\varphi} + \left(\tilde{\boldsymbol{b}} \cdot \nabla_\perp\right) \partial_\zeta \tilde{\varphi} \right\rangle^{(l=1)}\\
&\approx -\frac{L_zL_y}{(2\pi)^2} \int dk_{1y} \left\{ \frac{Ss^3 k_y^2 \left|\tilde{A}_{0\boldsymbol{k_1}}\right|^2}{\tau_A \nu_T |k_{1y}|} \times \right.\\
&\left. \frac{8\sqrt{\pi}\,|o_{\boldsymbol{k_1}}|^4}{w'^3} \right\} \left(\bar{\varphi}_{\boldsymbol{k}} + \zeta \partial_\zeta \bar{\varphi}_{\boldsymbol{k}}\right).
\end{aligned}$$

Since

$$\frac{[(b)+(c)]^{(l=0)}}{[(b)+(c)]^{(l=1)}} \sim \frac{|o_{\boldsymbol{k_1}}|^2}{w'^2} \sim \frac{1}{k_{1y}^2 w'^2} \ll 1, \tag{63}$$

we can use the $l = 0$ term to approximate the sum of correlation (b) and (c). After substituting equation

(50c), (61) and (62) into equation (50a), the large-scale vorticity equation becomes

$$\hat{H}_0\bar{\varphi}_{\boldsymbol{k}} = \hat{H}_1\bar{\varphi}_{\boldsymbol{k}}, \tag{64}$$

where

$$\hat{H}_0 = \frac{\partial^2}{\partial\zeta^2} - \frac{\gamma_{\boldsymbol{k}}\tau_A}{S}s^2\zeta^2k_y^2 + \frac{\gamma_{\boldsymbol{k}}\tau_Ak_y^2}{S}\left(\frac{\alpha g}{\gamma_{\boldsymbol{k}}^2}-1\right), \tag{65}$$

$$\begin{aligned}\hat{H}_1 =& \left[s^2\zeta^2k_y^2\left|\tilde{b}_x^2\right| - 2s\zeta k_y^2\left|\tilde{b}_x\tilde{b}_y\right| + k_y^2\left|\tilde{b}_y^2\right|\right]\\ &+\frac{L_zL_y}{(2\pi)^2}\int dk_{1y}\frac{Ss^3k_y^2\left|\tilde{A}_{0k_1}\right|^2}{\tau_A\nu_T\left|k_{1y}\right|}\frac{8\sqrt{\pi}\left|o_{\boldsymbol{k_1}}\right|^2}{w'}\zeta\partial_\zeta\\ &+\frac{\alpha g\tau_AD_Tk_y^4\left(1+s^2\zeta^2\right)}{S\gamma_{\boldsymbol{k}}^2} + \frac{\tau_A}{S}\nu_Tk_y^4\left(1+s^2\zeta^2\right)^2.\end{aligned} \tag{66}$$

Clearly the L.H.S of equation (65) is exactly the equation (13). By using perturbation theory, the first order growth rate correction $\gamma_{\boldsymbol{k}}^{(1)}$ is given by

$$\gamma_{\boldsymbol{k}}^{(1)} = \frac{\int_{-\infty}^{\infty}\bar{\varphi}_{\boldsymbol{k}}^{(0)}(\zeta)\,\hat{H}_1\bar{\varphi}_{\boldsymbol{k}}^{(0)}(\zeta)\,d\zeta}{\int_{-\infty}^{\infty}\bar{\varphi}_{\boldsymbol{k}}^{(0)}(\zeta)\left[\partial_{\gamma_k^{(0)}}\hat{H}_0\right]\bar{\varphi}_{\boldsymbol{k}}^{(0)}(\zeta)\,d\zeta}. \tag{67}$$

Plugging the expressions for $\hat{H}_0$, $\hat{H}_1$, and the 0th-order solution $\bar{\varphi}_{\boldsymbol{k}}^{(0)}$ into equation (67), the growth rate correction of the quasi-mode is

$$\begin{aligned}\gamma_{\boldsymbol{k}}^{(1)} =& \underbrace{-\frac{5}{6}\nu_Ts^2\Delta^2k_y^2\left(1+\frac{8}{5}\frac{1}{s^2\Delta^2}\right)}_{①}\\ &-\frac{1}{3}\frac{S}{\tau_A}\Big[\underbrace{\left|\tilde{b}_x^2\right|}_{②} - \underbrace{f\left|\tilde{b}_x^2\right|}_{③} + \underbrace{\frac{2}{s^2\Delta^2}\left|\tilde{b}_y^2\right|}_{④}\Big],\end{aligned} \tag{68}$$

where

$$\begin{aligned}f =& \frac{\left\langle\left(\tilde{\boldsymbol{b}}\cdot\nabla_\perp\partial_\zeta + \partial_\zeta\tilde{\boldsymbol{b}}\cdot\nabla_\perp\right)\tilde{\varphi}\right\rangle}{\left\langle(\tilde{\boldsymbol{b}}\cdot\nabla)(\tilde{\boldsymbol{b}}\cdot\nabla)\bar{\varphi}\right\rangle}\\ \sim& 8\underbrace{\frac{\nu_Tk_y^2}{\gamma_{\boldsymbol{k}}^{(0)}}}_{f_1}\underbrace{\frac{\alpha g}{\nu_T^2k_{1y}^4}}_{f_2}\underbrace{\frac{\left|o_{\boldsymbol{k_1}}\right|}{w'}}_{f_3}.\end{aligned} \tag{69}$$

The sign of $\gamma_{\boldsymbol{k}}^{(1)}$ will be determined in section 4.1. Another useful output of our calculation is the scaling of the turbulent viscosity ν_T. As discussed in section 3.2, the turbulent viscosity ν_T and the turbulent diffusivity D_T originate from the microturbulence. Hence, the scaling of ν_T and D_T can be calculated through the following closure model [48, 49]

$$\nu_T = \sum_{\boldsymbol{k_1}}\left|\tilde{v}_{x\boldsymbol{k_1}}\right|^2\tau_{\boldsymbol{k_1}}. \tag{70}$$

Here $\tau_{\boldsymbol{k_1}}$ is the turbulence correlation time, which can be estimated as $1/\gamma_{\boldsymbol{k_1}}$. Substituting equation (58) into equation (70) yields the following scaling of ν_T

$$\begin{aligned}\nu_T \cong& \left[\frac{L_zL_y}{(2\pi)^2}\int dk_{1y}\frac{s^3S^2\left|\tilde{A}_{\boldsymbol{k_1}}\right|^2}{\tau_A^2\left|k_{1y}\right|^3}\times\right.\\ &\left.\frac{4\sqrt{\pi}\left|o_{\boldsymbol{k_1}}\right|^2\bar{v}_{x\boldsymbol{k}}(0)^2}{w'(\alpha g)^{1/2}}\left\{\underbrace{2}_{\text{old}} + \underbrace{\left(\frac{k_{1y}o_{\boldsymbol{k_2}}^2}{k_y\delta_{\boldsymbol{k}}w'}\right)^2}_{\text{new}}\right\}\right]^{\frac{1}{3}}.\end{aligned} \tag{71}$$

4. Discussion and Conclusion

Given the fact that here a quasi-mode is a wave-packet consisting of localized resistive interchange modes, it's not surprising that this study would yield results somewhat similar to our prior research on the resistive interchange mode. *Nevertheless, due to the difference in the mode structure between the quasi-mode and the interchange mode, certain distinctions result.* In this section, we analyze the results obtained in section 3, with an emphasis on the *differences*. This paper concludes with a list of lessons that can deepen our comprehension of the effects of stochastic magnetic fields on the ballooning mode. In addition, suggested experiments and directions for future theoretical studies are provided.

4.1. Analysis of results

The term ① of the growth rate correction given by equation (68) is negative definite and proportional to ν_T. Except for an increment proportional to $1/(s\Delta)^2$, this term matches the first term of the growth rate correction for the resistive interchange mode given in our prior work [10]. The physics behind this term can be interpreted as the damping by the turbulent viscosity. Specifically, since the small-scale convective cells drive a turbulent background, the resultant turbulent viscosity ν_T and turbulent diffusivity D_T can promote mixing, thereby damping the growth of the quasi-mode. It can be observed that inside the braces of the scaling of ν_T, there are two terms labeled as "old" and "new" respectively. If only the "old" term is retained, the scaling of ν_T reverts to that given by equation (38) in [10]. In this study, due to the changes in the mode structure and the spatial scaling ordering, both $\tilde{b}_x$ and $\tilde{b}_y$ enter the calculation of the scaling of ν_T. This leads to the emergence of the "new" term in equation (71), which is positive. *The resultant new ν_T is larger than that obtained in our previous research on the resistive interchange mode.*

While term ② and term ④ are negative definite, term ③ is positive. Since term ③ stems from the

terms (b) and (c) in equation (50a), it implies that *the microturbulence has a destabilizing effect on the quasi-mode, in contrast to the case of the resistive interchange mode.* Again, this is due to the fact that the quasi-mode is much broader radially than the resistive interchange mode. Therefore, the sign of the sum of terms ②, ③, and ④ in equation (68) depends on the magnitude of parameter f, which is defined as the ratio of the sum of term (b) and term (c) to term (a) appearing in equation (50a). Equation (69) is an approximate expression for f, which is composed of three dimensionless factors, f_1, f_2, and f_3. The first factor f_1 is the ratio of the turbulent viscosity damping rate to the zeroth-order growth rate of the quasi-mode. As indicated in formula (48), due to the small magnitude of the magnetic perturbations, the effect of the stochastic magnetic field on the quasi-mode is considered as a small perturbation, which yields $\nu_T k_y^2 \ll \gamma_{\boldsymbol{k}}^{(0)}$ and thereby $f_1 \ll 1$. The second factor f_2 is equal to the square of the ratio of the 0th-order growth rate to the turbulent viscosity damping rate of the small-scale convective cells. As discussed in section (3.3), the growth of the small-scale convective cells is over-saturated by the turbulent viscosity and the turbulent diffusivity, which indicates $f_2 < 1$. As for the third factor f_3, given that we assume the magnitudes of $\tilde{b}_x$ and $\tilde{b}_y$ to be of the same order, the island width $o_{\boldsymbol{k_1}}$ is comparable to $1/k_{1y}$. Consequently, f_3 can be approximated as $1/(k_{1y}w')$, which is much smaller than unity, as the fast interchange approximation applies to the small-scale convective cells. The constant 8 multiplying these three factors originates from two sources: the Gaussian integrals in the calculation of the linear response of $\tilde{v}_x$ to $\tilde{\boldsymbol{b}}$, and the fact that the number of terms involving both $\tilde{\boldsymbol{b}}$ and $\tilde{v}_x$ (terms (b) and (c)) is double that of the terms involving $\tilde{\boldsymbol{b}}$ alone (term (a)) in equation (50a) . Since $f_1 \ll 1$, $f_2 < 1$, and $8f_3 \leq 1$ (or at least $\sim \mathcal{O}(1)$), it follows that $f \ll 1$, indicating the sum of term ②, ③ and ④ is also negative definite. *Therefore, we can conclude that the net effect of the stochastic magnetic field on the quasi-mode is to slow its growth.*

The stabilization effect of term ② and term ④ becomes clearer if only the term (a) are retained in equation (50a). Then the eigenmode equation for the quasi-mode reduces to

$$\frac{\partial^2}{\partial \zeta^2}\bar{v}_{x\boldsymbol{k}} - \frac{\rho_{\rm eff}\eta}{B_0^2}\gamma_{\boldsymbol{k}} k_y^2 s^2 \zeta^2 \bar{v}_{x\boldsymbol{k}} + \frac{\rho_0 \eta}{B_0^2}\frac{\alpha_{\rm eff} g}{\gamma_{\boldsymbol{k}}} k_y^2 \bar{v}_{x\boldsymbol{k}} = 0, \quad (72)$$

where expressions for effective plasma inertia $\rho_{\rm eff}$ and effective drive $\alpha_{\rm eff}$ are

$$\begin{aligned} \rho_{\rm eff} &= \rho_0 \left(1 + \frac{S}{\tau_A \gamma_{\boldsymbol{k}}}\left|\tilde{b}_x^2\right|\right) > \rho_0, \\ \alpha_{\rm eff} &= \alpha \left(1 - \frac{S\gamma_{\boldsymbol{k}}}{\tau_A \gamma_{\boldsymbol{k_1}}^2}\left|\tilde{b}_y^2\right|\right) < \alpha. \end{aligned} \quad (73)$$

The $|\tilde{b}_x \tilde{b}_y|$ cross term is omitted since it has no contribution to the growth rate correction. Here, $\rho_{\rm eff}$ and $\alpha_{\rm eff}$ are defined as the effective mass density and the effective density gradient, respectively. According to equation (73), *it is evident that stochastic magnetic fields can stabilize the mode growth by enhancing the effective plasma inertia and reducing the effective drive.* Furthermore, by balancing the stochastic bending term to the linear bending term, the critical island width for which this stabilization effect becomes significant is given as

$$o_{\boldsymbol{k_1}} \sim \delta_{\boldsymbol{k}} \left(\frac{k_y}{k_{1y}}\right)^{1/2}. \quad (74)$$

This result is a reminiscent of Rutherford's 1973 work on the nonlinear tearing mode [50]. In that paper, the growing perturbed magnetic field can generate a torque that drives the tearing mode against plasma inertia. But when the system enters the nonlinear regime, the nonlinear force induced by the perturbed magnetic field will produce another torque opposing the mode growth. The magnitudes of the torque produced by the linear and nonlinear forces become comparable when the island width is comparable to the width of the tearing layer, i.e., when $o_{\boldsymbol{k_1}} \sim \delta_{\boldsymbol{k}}$. As compared to Rutherford's model, equation (74) contains an additional factor of $(k_y/k_{1y})^{1/2}$, which is a footprint of the multi-scale nature of our model. The same criterion was also derived in our previous work.

4.2. Lessons learned for ballooning mode in a stochastic magnetic field

In this study, we constructed a comprehensive model for the dynamics of a low-$\boldsymbol{k}$ quasi-mode in a high-$\boldsymbol{k}$ stochastic magnetic field. For such an intrinsically multi-scale system, a standard procedure based on the quasi-linear theory is employed. By exploiting the resemblance between the quasi-mode and the ballooning mode, we can circumvent the difficulty posed by the differences in geometries between that used in theories of the ballooning mode and stochastic fields in a cylinder. Ultimately, we gain valuable physical insights into the dynamics of the ballooning mode in a stochastic magnetic field. These insights are consistent the existing simulations and experiments. The key takeaways from our study are:

(i) To maintain quasi-neutrality ($\nabla \cdot \boldsymbol{J} = 0$) at all scales, small-scale convective cells must be driven by the beat of the magnetic perturbations with the ballooning mode. In the simulation of the electrostatic resistive ballooning mode in a stochastic magnetic field by Beyer et al. [51], small-scale structures in the pressure fluctuation profile were observed. The emergence of these small-scale structures can be explained by the

microturbulence predicted by our theory. In addition, these small-scale convective cells could potentially allow for the possibility of enhanced nonlinear transfer by increasing the number of triad interactions. This picture provides another interpretation of the increase in the bicoherence of the pedestal temperature fluctuations in the stochastic layer, in addition to Waelbroeck et al.'s theory [52].

(ii) As indicated by equation (59), a non-trivial correlation develops between the velocity fluctuations $\tilde{v}_x$ and the magnetic perturbations $\tilde{\boldsymbol{b}}$. *Note that due to the change in the spatial ordering, a non-vanishing correlation* $\langle \tilde{b}_y \tilde{v}_x \rangle$ *appears in this work. Thus was absent in our previous work.* In other words, the microturbulence *"locks on"* to the externally prescribed stochastic magnetic field, and thus the edge plasma turbulence becomes more *"noisy"*. This theoretical prediction is consistent with the reduction of the Jensen-Shannon complexity of the temperature fluctuations during the RMP ELM suppression phase [21]. As previously discussed in section 1, the Jensen-Shannon complexity provides a metric for a system's predictability. Consequently, a decrease in the Jensen-Shannon complexity indicates an increase in the system's randomness. In other words, the chaotic behavior of the edge plasma turbulence is suppressed by an external noise, i.e., the stochastic magnetic field.

(iii) According to our discussion in section 4.1, it is reasonable to expect the stochastic magnetic field to impede the growth of the ballooning mode. This is also borne out by Beyer's simulation, in which a suppression of the large-scale fluctuations is observed [51]. More specifically, the stochastic magnetic field can slow the mode growth in three different ways: enhancing the effective plasma inertia (magnetic braking effect), reducing the effective drive, and boosting turbulent damping. *The second channel is newly discovered in this work.* The multi-scale nature of the system lowers the threshold for the magnitude of magnetic perturbations at which the magnetic braking effect becomes prominent, as compared with Rutherford's criterion [50].

(iv) In equation (3), mode coupling (represented by the convective term $\boldsymbol{v} \cdot \nabla \boldsymbol{v}$) is omitted to first order accuracy. However, the appearance of the microturbulence restores the time derivative ∂_t to a nonlinear operator $\partial_t + \tilde{\boldsymbol{v}} \cdot \nabla$, which is further renormalized as $\partial_t - \nu_T \nabla_\perp^2$. In other words, *the microturbulence drives a turbulent background in which plasma instabilities—including the ballooning mode—reside.* This conclusion remains unchanged from our previous research. Yet, the broad radial structure of the ballooning mode alters the influence of the microturbulence on the mode itself. Firstly, the magnitude of the turbulent viscosity ν_T and the turbulent diffusivity D_T is *larger* than what we obtained in our study on the radially-localized resistive interchange mode. Secondly, the electrostatic scattering caused by the microturbulence tends to destabilize the ballooning mode, which is *opposite to* our conclusion for the resistive interchange mode. This destabilizing effect has been proved to be much weaker than the magnetic braking effect.

4.3. Suggested experiments and future plan

While this paper focuses primarily on the quasi-mode, our findings are broadly applicable to other models, such as drift waves and ITG, as $\nabla \cdot \boldsymbol{J} = 0$ is a universal constraint for all types of modes. Thus, regardless of what the dominant mode at the edge is, when RMP is switched on, the microturbulence is inevitably driven, and the correlation between the microturbulence and the magnetic perturbations will be encountered. This further reinforces the validity of using our theory to explain the reduction in the complexity. However, as Jensen-Shannon complexity is a somewhat abstract concept, it is necessary to relate it to dynamical quantities, for practical purposes. Therefore, to validate our theory and enhance our understanding of plasma dynamics in a stochastic magnetic field, the following RMP experiments are suggested:

(i) Beam emission spectroscopy (BES) velocimetry is a high-resolution plasma diagnostic for plasma velocity fluctuations [53]. By using the BES velocimetry, we are able to calculate the of ratio of the turbulent heat flux to the total heat flux across the separatrix as a function of the strength of the magnetic perturbations (or, equivalently, the RMP coil current). The total heat flux could be obtained from the power budget. With the increase of the RMP coil current, the heat transport along the stochastic magnetic field would increase. At the same time, since we predict that the stochastic magnetic field can suppress the plasma instability, the turbulent heat flux would decrease. Hence, the decrease in the complexity of the edge turbulence should be accompanied by a reduction in the ratio of turbulent heat flux to the total heat flux.

(ii) Since Choi et al. used the electron cyclotron emission imaging (ECEI) as their pedestal turbulence diagnostic [54], their complexity analysis is based on electron temperature fluctuations. It might be

enlightening to perform a similar analysis for the data of velocity fluctuations collected from BES velocimetry during both the RMP ELM suppression phase and the natural ELM-free phase. This is not only complementary to Choi's results, but also a straightforward verification of our theory. Considering both Choi's observations and the non-trivial correlation $\langle \tilde{v}_x \tilde{\boldsymbol{b}} \rangle$ in our theory, a decrease in the Jensen-Shannon complexity in the RMP ELM suppression phase is anticipated.

(iii) Direct examination of the presence of the correlation $\langle \tilde{v}_x \tilde{\boldsymbol{b}} \rangle$ also warrants further investigation. Using the velocity fluctuations gathered from BES and the magnetic fluctuation obtained from either simulations or experiments, we can calculate the correlation between $\tilde{v}_x$ and $\tilde{\boldsymbol{b}}$, and compare it to our theoretical prediction given by equation (59).

In addition to the experiments suggested above, two potential directions for future theoretical research have also been identified.

(i) One may notice that zonal flow, a critical player in L-H transition, is missing from our model. In fact, it has been found that the stochastic magnetic field can indeed affect the zonal flow and the radial electric field [8, 55]. Many phenomena in RMP experiments, such the increase in the L-H transition power threshold, can be attributed to the weakening of the shear flow. Hence, our next step will be to incorporate the zonal flow into our model. As is well known, zonal flow is driven by the Reynolds stress, which is represented as $\langle \tilde{v}_x \tilde{v}_y \rangle$. A non-vanishing Reynolds stress indicates a non-trivial correlation between k_x and k_y, i.e., $\langle k_x k_y \rangle \neq 0$. In the predator-prey model for zonal flow and drift wave turbulence [56], a non-trivial $\langle k_x k_y \rangle$ can develop from an initial weak velocity shear, i.e.,
$$\frac{dk_x}{dt} = -\langle v_E \rangle' k_y. \tag{75}$$
For years velocity shear has been recognized as the primary seed of zonal flow. However, k_x and k_y can also develop a non-trivial correlation from magnetic shear. With the presence of the magnetic shear, we have the equation
$$\frac{dk_x}{dz} = -sk_y, \tag{76}$$
which is similar in form to equation (75). This fact gives us some insights into future studies in this direction.

(ii) In section 3.3, the quasi-linear theory [57] is utilized to obtain the linear response of $\tilde{v}_x$ to $\tilde{\boldsymbol{b}}$. While doing so, we must be aware that the validity of the quasi-linear theory requires
$$Ku \approx \left(\frac{l_{ac}}{l_c}\right)^2 < 1. \tag{77}$$
Here Ku is a dimensionless number known as Kubo number. l_{ac} and l_c denote the auto-correlation length and decorrelation length of the stochastic magnetic field, respectively. However, the reality in tokamak is $Ku \sim 1$ [58]. Currently, almost all theories concerning stochastic magnetic fields are limited to the case where $Ku < 1$, while the $Ku > 1$ case is rarely studied. Therefore, another potential direction for future research is to investigate the effects of the stochastic magnetic fields on plasma instabilities and turbulence in the $Ku \gg 1$ regime. Then, by decreasing Ku, we can approach the $Ku \sim 1$ regime asymptotically. In such cases, the quasi-linear theory is no longer available so we must look for new paradigms. Taylor and McNamara's work on 2D guiding center plasma and purely random array of discrete charged rods [59, 60] could be a good starting point. The behavior of their system is more like percolation process rather than diffusion process. Hence, it would be beneficial to seek inspiration from percolation theory [61, 62]. This work is expected to enhance our understanding of the actual situation by providing a perspective entirely different from the $ku < 1$ case.

(iii) As discussed in section 3.3, we use the non-trivial correlation $\langle \tilde{v}_x \tilde{\boldsymbol{b}} \rangle$ and the idea of the suppression of the instability characteristic of a chaotic system by external noise to explain the reduction in the complexity of the edge turbulence in the RMP ELM suppression phase. But we should recognize that the stochastic magnetic field is actually *not noise, but deterministic chaos*. Therefore, a deeper approach to justify our claim is to study how one chaotic system can affect the complexity of another. For simplicity, we can take 1D as a starting point. Suppose there are two different chaotic systems with different Lyapunov exponents, each producing a signal. We can then calculate the Jensen-Shannon complexity for each of these signals, as well as for their superposition. The point is to see whether the complexity of this superposed signal is reduced relative to the complexity of each individual signal, under certain conditions. This numerical experiment can be easily done and would serve as a further justification of our conclusion.

Acknowledgments

We acknowledge the valuable discussion with Minjun Choi during the 6th Asia-Pacific Transport Working Group meeting. We also thank T S Hahm for the instructive discussion with him during his visit to UC San Diego. This research was supported by the

U.S. Department of Energy under Award Number DE-FG02-04ER54738.

Appendix A. Calculation of the Jensen-Shannon complexity

Given a series of data with N data points, we can use a sliding window of length d to capture the segments of the data. For instance, as shown in figure A1, when $d = 3$, consecutive segments such as (a_1, a_2, a_3), (a_2, a_3, a_4), (a_3, a_4, a_5) can be extracted. We can then map an arbitrary segment $(s) \equiv (a_{s-2}, a_{s-1}, a_s)$ at time s to an "ordinary" pattern, which is a permutation $\pi = (b_1, b_2, b_3)$ of $(0, 1, 2)$ defined by $(a_{s-b_3} \leq a_{s-b_2} \leq a_{s-b_1})$. If $a_2 = 7$, $a_3 = 8$, $a_4 = 9$, $a_5 = 6$, then the corresponding "ordinary patterns" of (a_2, a_3, a_4) and (a_3, a_4, a_5) are $(0, 1, 2)$ and $(1, 2, 0)$, respectively. In the case of $d = 3$, there are $d! = 6$ possible permutations. By executing this mapping to all the segments, we can obtain a probability distribution $P = \{p(\pi)\}$ defined by

$$p(\pi) = \frac{\#\{s | d \leq s \leq N;\ \mathrm{map}(s) = \pi\}}{N - d + 1}, \tag{A.1}$$

where # is the number of segments satisfying condition inside the braces. For the distribution function to be meaningful, N should be significantly larger than $d!$. Using this distribution function, the normalized Shannon entropy is equal to

$$H[P] = -\sum_{i=1}^{d!} p_i \ln(p_i)/S_{\max}, \tag{A.2}$$

where $S_{\max} = \ln(d!)$ is the entropy of the uniform distribution $P_e = \{p_i = 1/d!\}$. And the Jensen-Shannon divergence is calculated as

$$Q = Q_0\{S[(P + P_e)/2] - S[P]/2 - S[P_e]/2\}, \tag{A.3}$$

where Q_0 is a normalization constant. The Jensen-Shannon complexity C_{JS} is defined by equation (1), namely, the product of H and Q.

In Choi et al.'s work, C_{JS} is rescaled by the complexity of fractional Brownian noise or fractional Gaussian noise C_0 as

$$\hat{C} = \frac{C_{\mathrm{JS}} - C_0}{|C_{\mathrm{bdry}} - C_0|}, \tag{A.4}$$

where C_{bdry} is the maximum (if $C_{\mathrm{JS}} > C_0$) or minimum (if $C_{JS} < C_0$) Jensen-Shannon complexity at the given H. The rescaled $\hat{C}$ ranges from -1 to 1.

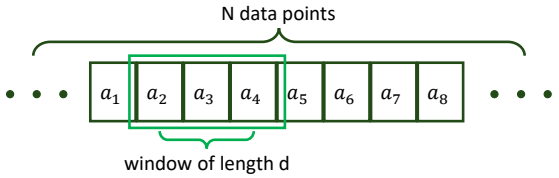

Figure A1. The sketch of the calculation of the Jensen-Shannon complexity for signal data

Appendix B. Expressions for the operators in this work

The derivatives in twisted slicing coordinate are

$$\begin{aligned}
\frac{\partial}{\partial x} &= \frac{\partial}{\partial \xi} - s\zeta\frac{\partial}{\partial \chi}, \\
\frac{\partial}{\partial y} &= \frac{\partial}{\partial \chi}, \\
\frac{\partial}{\partial z} &= \frac{\partial}{\partial \zeta} - s\xi\frac{\partial}{\partial \chi}.
\end{aligned} \tag{B.1}$$

The expressions for the operators used in this paper are

$$\begin{aligned}
\nabla^2 &= \frac{\partial^2}{\partial \xi^2} + \frac{\partial^2}{\partial \chi^2} + \frac{\partial^2}{\partial \zeta^2} \\
&+ s^2\xi^2\frac{\partial^2}{\partial \chi^2} + s^2\zeta^2\frac{\partial^2}{\partial \chi^2} - 2s\xi\frac{\partial^2}{\partial \chi \partial \zeta} - 2s\zeta\frac{\partial^2}{\partial \xi \partial \chi}, \\
\nabla_\perp^2 &= \frac{\partial^2}{\partial \xi^2} + \frac{\partial^2}{\partial \chi^2} + s^2\zeta^2\frac{\partial^2}{\partial \chi^2} - 2s\zeta\frac{\partial^2}{\partial \xi \partial \chi}, \\
\frac{\partial^2}{\partial y^2} + \frac{\partial^2}{\partial z^2} &= \frac{\partial^2}{\partial \chi^2} + \frac{\partial^2}{\partial \zeta^2} \\
&+ s^2\xi^2\frac{\partial^2}{\partial \chi^2} - 2s\xi\frac{\partial^2}{\partial \chi \partial \zeta}, \\
\boldsymbol{B_0} \cdot \nabla &= \frac{\partial}{\partial z} + sx\frac{\partial}{\partial y} = \frac{\partial}{\partial \zeta}, \\
\tilde{\boldsymbol{b}} \cdot \nabla_\perp &= \tilde{b}_x\left(\frac{\partial}{\partial \xi} - s\zeta\frac{\partial}{\partial \chi}\right) + \tilde{b}_y\frac{\partial}{\partial \chi}.
\end{aligned} \tag{B.2}$$

References

[1] T. Eich, A.W. Leonard, R.A. Pitts, W. Fundamenski, R.J. Goldston, T.K. Gray, A. Herrmann, A. Kirk, A. Kallenbach, O. Kardaun, A.S. Kukushkin, B. LaBombard, R. Maingi, M.A. Makowski, A. Scarabosio, B. Sieglin, J. Terry, A. Thornton, ASDEX Upgrade Team, and JET EFDA Contributors. Scaling of the tokamak near the scrape-off layer h-mode power width and implications for iter. *Nuclear Fusion*, 53(9):093031, aug 2013.

[2] Todd E Evans, Richard A Moyer, Keith H Burrell, Max E Fenstermacher, Ilon Joseph, Anthony W Leonard, Thomas H Osborne, Gary D Porter, Michael J Schaffer, Philip B Snyder, Paul R Thomas, Jonathan G Watkins, and William P West. Edge stability and transport control with resonant magnetic perturbations in collisionless tokamak plasmas. *Nature Physics*, 2(6):419–423, June 2006.

[3] Y. Sun, Y. Liang, Y. Q. Liu, S. Gu, X. Yang, W. Guo, T. Shi, M. Jia, L. Wang, B. Lyu, C. Zhou, A. Liu, Q. Zang, H. Liu, N. Chu, H. H. Wang, T. Zhang, J. Qian, L. Xu, K. He, D. Chen, B. Shen, X. Gong, X. Ji, S. Wang, M. Qi, Y. Song, Q. Yuan, Z. Sheng, G. Gao, P. Fu, and B. Wan. Nonlinear transition from mitigation to suppression of the edge localized mode with resonant magnetic perturbations in the east tokamak. *Phys. Rev. Lett.*, 117:115001, Sep 2016.

[4] F. Ryter, S.K. Rathgeber, L. Barrera Orte, M. Bernert, G.D. Conway, R. Fischer, T. Happel, B. Kurzan, R.M. McDermott, A. Scarabosio, W. Suttrop, E. Viezzer, M. Willensdorfer, E. Wolfrum, and the ASDEX Upgrade Team. Survey of the h-mode power threshold and transition physics studies in asdex upgrade. *Nuclear Fusion*, 53(11):113003, sep 2013.

[5] Y. In, J.-K. Park, Y.M. Jeon, J. Kim, G.Y. Park, J.-W. Ahn, A. Loarte, W.H. Ko, H.H. Lee, J.W. Yoo, J.W. Juhn, S.W. Yoon, H. Park, and 3D Physics Task Force in KSTAR. Enhanced understanding of non-axisymmetric intrinsic and controlled field impacts in tokamaks. *Nuclear Fusion*, 57(11):116054, aug 2017.

[6] L. Schmitz, D.M. Kriete, R.S. Wilcox, T.L. Rhodes, L. Zeng, Z. Yan, G.R. McKee, T.E. Evans, C. Paz-Soldan, P. Gohil, B. Lyons, C.C. Petty, D. Orlov, and A. Marinoni. L–h transition trigger physics in iter-similar plasmas with applied n=3 magnetic perturbations. *Nuclear Fusion*, 59(12):126010, sep 2019.

[7] Chang-Chun Chen and Patrick H. Diamond. Potential vorticity mixing in a tangled magnetic field. *The Astrophysical Journal*, 892(1):24, mar 2020.

[8] Weixin Guo, Min Jiang, Patrick H Diamond, Chang-Chun Chen, Mingyun Cao, Hanhui Li, and Ting Long. Theory of mean exb shear in a stochastic magnetic field: ambipolarity breaking and radial current. *Plasma Physics and Controlled Fusion*, 64(12):124001, oct 2022.

[9] Chang-Chun Chen, Patrick H. Diamond, Rameswar Singh, and Steven M. Tobias. Potential vorticity transport in weakly and strongly magnetized plasmas. *Physics of Plasmas*, 28(4):042301, 04 2021.

[10] Mingyun Cao and P H Diamond. Instability and turbulent relaxation in a stochastic magnetic field. *Plasma Physics and Controlled Fusion*, 64(3):035016, feb 2022.

[11] G.R. McKee, Z. Yan, C. Holland, R.J. Buttery, T.E. Evans, R.A. Moyer, S. Mordijck, R. Nazikian, T.L. Rhodes, O. Schmitz, and M.R. Wade. Increase of turbulence and transport with resonant magnetic perturbations in elm-suppressed plasmas on diii-d. *Nuclear Fusion*, 53(11):113011, sep 2013.

[12] Christoph Bandt, Gerhard Keller, and Bernd Pompe. Entropy of interval maps via permutations. *Nonlinearity*, 15(5):1595, aug 2002.

[13] Karsten Keller and Mathieu Sinn. Kolmogorov–sinai entropy from the ordinal viewpoint. *Physica D: Nonlinear Phenomena*, 239(12):997–1000, 2010.

[14] O. A. Rosso, H. A. Larrondo, M. T. Martin, A. Plastino, and M. A. Fuentes. Distinguishing noise from chaos. *Phys. Rev. Lett.*, 99:154102, Oct 2007.

[15] Francesco Serinaldi, Luciano Zunino, and Osvaldo A. Rosso. Complexity–entropy analysis of daily stream flow time series in the continental united states. *Stochastic Environmental Research and Risk Assessment*, 28(7):1685–1708, Oct 2014.

[16] Luciano Zunino, Massimiliano Zanin, Benjamin M. Tabak, Darío G. Pérez, and Osvaldo A. Rosso. Complexity-entropy causality plane: A useful approach to quantify the stock market inefficiency. *Physica A: Statistical Mechanics and its Applications*, 389(9):1891–1901, 2010.

[17] Ernesto Estevez-Rams, Ania Mesa-Rodriguez, and Daniel Estevez-Moya. Complexity-entropy analysis at different levels of organisation in written language. *PLOS ONE*, 14(5):1–16, 05 2019.

[18] J E Maggs and G J Morales. Permutation entropy analysis of temperature fluctuations from a basic electron heat transport experiment. *Plasma Physics and Controlled Fusion*, 55(8):085015, jun 2013.

[19] J E Maggs, T L Rhodes, and G J Morales. Chaotic density fluctuations in l-mode plasmas of the diii-d tokamak. *Plasma Physics and Controlled Fusion*, 57(4):045004, mar 2015.

[20] Z. Zhu, A. E. White, T. A. Carter, S. G. Baek, and J. L. Terry. Chaotic edge density fluctuations in the Alcator C-Mod tokamak. *Physics of Plasmas*, 24(4):042301, 04 2017.

[21] Minjun J. Choi, Jae-Min Kwon, Juhyung Kim, Tongnyeol Rhee, Jun-Gyo Bak, Giwook Shin, Hyun-Seok Kim, Hogun Jhang, Kimin Kim, Gunsu S. Yun, Minwoo Kim, SangKyeun Kim, Helen H. Kaang, Jong-Kyu Park, Hyung Ho Lee, Yongkyoon In, Jaehyun Lee, Minho Kim, Byoung-Ho Park, and Hyeon K. Park. Stochastic fluctuation and transport of tokamak edge plasmas with the resonant magnetic perturbation field. *Physics of Plasmas*, 29(12):122504, 12 2022.

[22] Harold P. Furth, John Killeen, and Marshall N. Rosenbluth. Finite-Resistivity Instabilities of a Sheet Pinch. *The Physics of Fluids*, 6(4):459–484, 04 1963.

[23] Bruno Coppi, John M. Greene, and John L. Johnson. Resistive instabilities in a diffuse linear pinch. *Nuclear Fusion*, 6(2):101, jun 1966.

[24] B. A. Carreras, V. E. Lynch, L. Garcia, and P. H. Diamond. Resistive pressure-gradient-driven turbulence with self-consistent flow profile evolution. *Physics of Fluids B: Plasma Physics*, 5(5):1491–1505, 05 1993.

[25] J. W. Connor, R. J. Hastie, H. R. Wilson, and R. L. Miller. Magnetohydrodynamic stability of tokamak edge plasmas. *Physics of Plasmas*, 5(7):2687–2700, 07 1998.

[26] Roscoe B White. *The Theory of Toroidally Confined Plasmas*. PUBLISHED BY IMPERIAL COLLEGE PRESS AND DISTRIBUTED BY WORLD SCIENTIFIC PUBLISHING CO., 2006.

[27] R. Fitzpatrick and T. C. Hender. The interaction of resonant magnetic perturbations with rotating plasmas. *Physics of Fluids B: Plasma Physics*, 3(3):644–673, 03 1991.

[28] Allen H. Boozer. What is a stellarator? *Physics of Plasmas*, 5(5):1647–1655, 05 1998.

[29] C. C. Hegna and N. Nakajima. On the stability of Mercier and ballooning modes in stellarator configurations. *Physics of Plasmas*, 5(5):1336–1344, 05 1998.

[30] C. C. Hegna and S. R. Hudson. Ideal magnetohydrodynamic ballooning stability boundaries in three-dimensional equilibria. *Physics of Plasmas*, 9(5):2014–2019, 04 2002.

[31] C.C. Hegna. Healing of magnetic islands in stellarators by plasma flow. *Nuclear Fusion*, 51(11):113017, oct 2011.

[32] C. C. Hegna. Plasma flow healing of magnetic islands in stellaratorsa). *Physics of Plasmas*, 19(5):056101, 03 2012.

[33] Yao Zhou, N.M. Ferraro, S.C. Jardin, and H.R. Strauss. Approach to nonlinear magnetohydrodynamic simulations in stellarator geometry. *Nuclear Fusion*, 61(8):086015, jul 2021.

[34] S. R. Hudson and J. Breslau. Temperature contours and ghost surfaces for chaotic magnetic fields. *Phys. Rev. Lett.*, 100:095001, Mar 2008.

[35] Elizabeth J. Paul, Stuart R. Hudson, and Per Helander. Heat conduction in an irregular magnetic field. part 2. heat transport as a measure of the effective non-integrable volume. *Journal of Plasma Physics*, 88(1):905880107, 2022.

[36] K. Matsumoto and I. Tsuda. Noise-induced order. *Journal of Statistical Physics*, 31(1):87–106, Apr 1983.

[37] K. V. Roberts and J. B. Taylor. Gravitational Resistive Instability of an Incompressible Plasma in a Sheared Magnetic Field. *The Physics of Fluids*, 8(2):315–322, 02 1965.

[38] John William Connor, R. J. Hastie, and John Bryan Taylor. High mode number stability of an axisymmetric toroidal plasma. *Proceedings of the Royal Society of London. A. Mathematical and Physical Sciences*, 365(1720):1–17, 1979.

[39] W.M. Tang. Microinstability theory in tokamaks. *Nuclear Fusion*, 18(8):1089, aug 1978.

[40] J W Connor, R J Hastie, and J B Taylor. Stability of general plasma equilibria. iii. *Plasma Physics*, 22(7):757, jul 1980.

[41] Mitsuru Kikuchi and Masafumi Azumi. *Fundamentals of Ballooning Modes in Tokamak*, pages 157–173. Springer International Publishing, Cham, 2015.

[42] P Ricci, F D Halpern, S Jolliet, J Loizu, A Mosetto, A Fasoli, I Furno, and C Theiler. Simulation of plasma turbulence in scrape-off layer conditions: the gbs code, simulation results and code validation. *Plasma Physics and Controlled Fusion*, 54(12):124047, nov 2012.

[43] B. A. Carreras and P. H. Diamond. Thermal diffusivity induced by resistive pressure-gradient-driven turbulence. *Physics of Fluids B: Plasma Physics*, 1(5):1011–1017, 05 1989.

[44] H. R. Strauss. Nonlinear, three-dimensional magnetohydrodynamics of noncircular tokamaks. *The Physics of Fluids*, 19(1):134–140, 01 1976.

[45] Y-K.M. Peng and D.J. Strickler. Features of spherical torus plasmas. *Nuclear Fusion*, 26(6):769, jun 1986.

[46] Patrick H. Diamond, Sanae-I. Itoh, and Kimitaka Itoh. *Modern Plasma Physics*, volume 1. Cambridge University Press, 2010.

[47] Philip M. Morse, Herman Feshbach, and E. L. Hill. Methods of Theoretical Physics. *American Journal of Physics*, 22(6):410–413, 09 1954.

[48] T. H. Dupree. A Perturbation Theory for Strong Plasma Turbulence. *The Physics of Fluids*, 9(9):1773–1782, 09 1966.

[49] B. A. Carreras, L. Garcia, and P. H. Diamond. Theory of resistive pressure-gradient-driven turbulence. *The Physics of Fluids*, 30(5):1388–1400, 05 1987.

[50] P. H. Rutherford. Nonlinear growth of the tearing mode. *The Physics of Fluids*, 16(11):1903–1908, 11 1973.

[51] P. Beyer, X. Garbet, and P. Ghendrih. Tokamak turbulence with stochastic field lines. *Physics of Plasmas*, 5(12):4271–4279, 12 1998.

[52] F. L. Waelbroeck, J. W. Connor, and H. R. Wilson. Finite larmor-radius theory of magnetic island evolution. *Phys. Rev. Lett.*, 87:215003, Nov 2001.

[53] G. McKee, R. Ashley, R. Durst, R. Fonck, M. Jakubowski, K. Tritz, K. Burrell, C. Greenfield, and J. Robinson. The beam emission spectroscopy diagnostic on the DIII-D tokamak. *Review of Scientific Instruments*, 70(1):913–916, 01 1999.

[54] G. S. Yun, W. Lee, M. J. Choi, J. Lee, M. Kim, J. Leem, Y. Nam, G. H. Choe, H. K. Park, H. Park, D. S. Woo, K. W. Kim, C. W. Domier, Jr. Luhmann, N. C., N. Ito, A. Mase, and S. G. Lee. Quasi 3D ECE imaging system for study of MHD instabilities in KSTARa). *Review of Scientific Instruments*, 85(11):11D820, 07 2014.

[55] M. Leconte, P.H. Diamond, and Y. Xu. Impact of resonant magnetic perturbations on zonal modes, drift-wave turbulence and the l–h transition threshold. *Nuclear Fusion*, 54(1):013004, nov 2013.

[56] P H Diamond, S-I Itoh, K Itoh, and T S Hahm. Zonal flows in plasma—a review. *Plasma Physics and Controlled Fusion*, 47(5):R35, apr 2005.

[57] A.A. Vedenov, E.P. Velikhov, and R.Z. Sagdeev. Nonlinear oscillations of rarified plasma. *Nuclear Fusion*, 1(2):82, mar 1961.

[58] Wonjun Lee. Turbulence analysis by estimating kubo number in l-mode, h-mode, and elms-suppressed h-mode plasmas. Master's thesis, Korea Advanced Institute of Science and Technology, 2019.

[59] J. B. Taylor and B. McNamara. Plasma Diffusion in Two Dimensions. *The Physics of Fluids*, 14(7):1492–1499, 07 1971.

[60] J. B. Taylor and W. B. Thompson. Fluctuations in guiding center plasma in two dimensions. *The Physics of Fluids*, 16(1):111–117, 01 1973.

[61] D. Stauffer. Scaling theory of percolation clusters. *Physics Reports*, 54(1):1–74, 1979.

[62] D. Bernard, G. Boffetta, A. Celani, and G. Falkovich. Conformal invariance in two-dimensional turbulence. *Nature Physics*, 2(2):124–128, Feb 2006.